



Rigid and deformable bodies in nematic liquid crystals

Thomas G. J. Chandler ^{1,*} and Saverio E. Spagnolie ^{1,2,†}¹*Department of Mathematics, University of Wisconsin–Madison, Madison, Wisconsin 53706, USA*²*Department of Chemical and Biological Engineering, University of Wisconsin–Madison, Madison, Wisconsin 53706, USA*

(Received 5 August 2024; accepted 21 October 2024; published 20 November 2024)

A nematic liquid crystal, a phase of matter composed of rodlike molecules, exhibits a tendency towards uniform molecular alignment. Bodies inserted into such a fluid can disturb this orientational order, resulting in elastic stresses bound in the bulk fluid and exerted on the body surfaces, even at equilibrium. One avenue of energy relaxation is by a change in the immersed particle positions and orientations, leading to elastic forces and torques that bodies exert on each other through the fluid. Soft particles offer an additional means of relaxation, deformation, which in turn can modify particle interactions through the LC medium. We review classical work on rigid particles and their interactions in nematic liquid crystals and more recent work on the shapes and interactions of deformable bodies in LCs. In addition to experimental findings, a number of common mathematical modeling techniques, both in terms of a director field \mathbf{n} and a second-order tensor field \mathbf{Q} , are introduced throughout, including derivations of body forces and torques and, of particular use in the study of deformable media in LCs, surface tractions and moments.

DOI: [10.1103/PhysRevFluids.9.110511](https://doi.org/10.1103/PhysRevFluids.9.110511)

I. INTRODUCTION

The study of liquid crystals (LCs) has come a long way since 1888, when botanist Friedrich Reinitzer first observed a peculiar behavior using cholesterol extracted from a carrot [1]. While heating the molecular suspension, the fluid properties changed not at one critical temperature, but at two. First observed was a change in the material properties, solids melting into a cloudy white fluid, Fig. 1(a). At a yet higher temperature, the optical properties were found to change from cloudy white to clear. This was very puzzling; the physics of phase change, understood as it was at the time, would demand that material and optical (and any other) properties should change at the same temperature. Reinitzer sent a letter to crystallographer Otto Lehmann, who could verify the “two states of matter” more directly with a microscope fitted with polarized lenses. So began a decades-long journey towards the development of liquid crystal physics, and the appreciation that molecular orientational order (which may change how light passes through the medium, for instance) can be independent of positional order and solidification.

Among the great variety of new phases uncovered during this era were so-called nematic liquid crystals. A nematic LC is a state of soft matter in which rodlike molecules possess orientational order but no positional order [2]. These molecules might compose the fluid entirely, showing phase changes as a function of temperature (thermotropic LCs) or may be immersed in a solvent, showing phase changes as a function of temperature and concentration [lyotropic LCs; Fig. 1(b)]. The elongated rodlike structures might actually be composed of stacks of smaller molecules (chromonic

*Contact author: tgchandler@wisc.edu†Contact author: spagnolie@math.wisc.edu

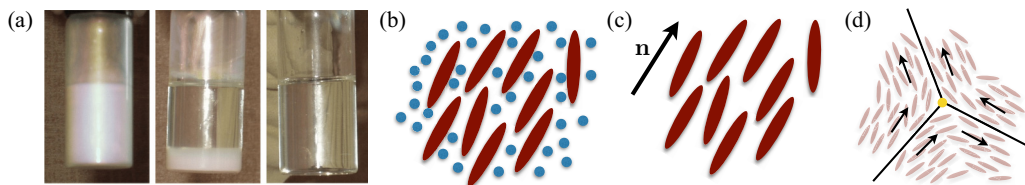


FIG. 1. (a) As temperature increases above a “second” melting point, a liquid crystal sample loses its orientational order and becomes optically translucent. Reproduced from Ref. [36]. (b) In a lyotropic nematic LC, rodlike molecules are immersed in a solvent bath, and phase changes can occur due to a combination of temperature and concentration changes. (c) The average local molecular orientation is represented as a director field $\mathbf{n}(\mathbf{x}, t)$. Theoretical treatments must respect $\mathbf{n} \mapsto -\mathbf{n}$ symmetry. (d) A $-1/2$ topological defect corresponds to a 180° clockwise rotation in the director angle, on traversing a connected path around a point in the counterclockwise direction.

LCs). Due to the temperature dependence of the stack lengths, the viscosities of chromonic LCs can depend strongly on temperature [3]. A popular LC for liquid-crystal display applications is 5CB [4], which is thermotropic; and a popular LC for experiments involving biological cells is disodium cromoglycate (DSCG), which is lyotropic and chromonic [3].

Some biological fluids, such as mucus [5,6] and biofilms [7–10], also exhibit anisotropy, which in turn can affect pathogen transport [11–16]. Biological systems composed of much larger elongated structures, for instance colonies of motile *Escherichia coli* [17,18], *Bacillus subtilis* [19], and *Myxococcus* cells [20], have shown similar phase transitions to orientational order. Inside the cell, biofilaments like microtubules [21,22] and actin [23,24] also reveal emergent and functionally important anisotropic structure, as does chromatin, the functional form of DNA, which self-organizes into distinct compartments where internal nematic order arises through active forcing [25–27]. Such “active suspensions” or “active nematic” fluids have been the subject of intense study since the early 2000s [28–30]. Medical diagnostics are one of the many potential applications on the horizon [31–33].

The orientational order of LCs results in an anisotropic, viscoelastic stress response to deformation and flow. In a uniaxial LC, the average local molecular orientation in a small control volume is commonly represented as a director field $\mathbf{n}(\mathbf{x}, t)$, with spatial position \mathbf{x} , time t , and $|\mathbf{n}(\mathbf{x}, t)| = 1$ [Fig. 1(c)]. A uniform director field is an energy minimizing ground state, and small spatial variations in the director field result in an elastic stress response to deformation. Among the most alluring features of LCs are the almost immediate appearance of topological singularities in a variety of settings which have associated “charges” satisfying topological conservation laws [34,35]. Figure 1(d) shows a “ $-1/2$ ” topological defect, which corresponds to a 180° clockwise rotation in the director angle upon traversing a connected path around a point in the opposite (counterclockwise) direction. The name “nematic” is due to the threadlike nature of disclination lines connecting such topological defects (the Greek word for thread is $\nu\eta\mu\alpha$).

Left unconstrained, a nematic LC tends to relax towards a uniform orientation. Potentially frustrating this equilibrium configuration are energetically preferred molecular orientations at confining or immersed boundaries [37]. When rigid particles are immersed in an anisotropic fluid, the director field is generically disturbed, and elastic energy is stored in the fluid at equilibrium. One means by which that elastic energy may be relaxed is if the immersed particle is deformable. An equilibrium state is then achieved through a balance between the energy stored in the fluid and the energy stored by the stretched or otherwise deformed body. Such stretching has much in common with LC droplets, or “tactoids,” which are observed to elongate due to a competition between bulk elastic stresses and surface tension [38]. Elastic shells, including vesicles [39–41] and blood cells [42], introduce other physical penalties, such as shear elasticity, but reveal similarly elongated structures. Other deformations are also possible, depending on the details of the molecular

anchoring conditions [40]. Since body deformation reduces the energy stored in the environment, elastic interactions between two or more immersed bodies is also expected to be affected by particle deformability.

In this review, we will begin by recalling some of the classical features of LCs with one or many rigid immersed bodies. Our focus will be confined to the setting where the bodies are large when compared to the molecular scale, where continuum models for the LC are expected to be most accurate. LC configurations due to immersed rigid particles, and the associated topological defects and stresses, represent a base state around which energy-reducing deformations may be better understood. We then turn to one or many deformable bodies, first by recalling classical works on LC droplets (“tactoids”), then turning to soft deformable media, including recent work on the stretching of soft vesicles and cells by an LC medium, nematic surfaces, and multiple body interactions. Various mathematical modeling techniques, and terminology, are discussed throughout. Classical models constructed on the director field, \mathbf{n} , as well as on a second-order \mathbf{Q} tensor are discussed, and body forces and torques at equilibrium are derived. In addition, and of particular need when studying the shapes of soft media in contact with a bulk LC, we include derivations of LC surface tractions and moments associated with different LC models. We conclude with a discussion which touches on numerical methods, active particles and stresses, and future directions of inquiry.

A. Mathematical modeling—Free energy density

In the classical Ericksen model of a nematic liquid crystal, mechanical stresses are based on variations of the Oseen-Frank free energy density, \mathcal{F} , which is defined in terms of the director field \mathbf{n} and respects $\mathbf{n} \mapsto -\mathbf{n}$ symmetry. This energy is given by

$$\begin{aligned} \mathcal{F}(\mathbf{n}, \nabla \mathbf{n}) = & \frac{K_1}{2} (\nabla \cdot \mathbf{n})^2 + \frac{K_2}{2} (\mathbf{n} \cdot \nabla \times \mathbf{n})^2 + \frac{K_3}{2} |\mathbf{n} \times (\nabla \times \mathbf{n})|^2 \\ & - \frac{K_{24}}{2} \nabla \cdot [\mathbf{n}(\nabla \cdot \mathbf{n}) + \mathbf{n} \times (\nabla \times \mathbf{n})], \end{aligned} \quad (1)$$

where K_1 , K_2 , K_3 , and K_{24} are the Frank elastic constants (with units of force) and gradients are defined with respect to spatial position. The first three terms penalize the continuous deformations of splay ($\nabla \cdot \mathbf{n}$), twist ($\mathbf{n} \cdot \nabla \times \mathbf{n}$), and bend $|\mathbf{n} \times (\nabla \times \mathbf{n})|$ [2,43]. The fourth term, with constant K_{24} , has components already present in the first three terms, plus an additional penalty for a fourth independent mode, biaxial splay; for a detailed discussion of this term in particular see Ref. [44]. This fourth term is often omitted, as it can be absorbed into a surface energy after integrating over the domain. Note that these elastic constants are defined differently across the literature, so caution is advised. These constants must also obey certain inequalities, else the system is mathematically unstable [44–46]. However, it was noted by Selinger [44] that the arguments used by Ericksen [45] to develop these inequalities were circular and that the standard inequalities can be violated by certain LCs. Characteristic values of these constants are on the order of 10^{-6} dyn, though K_2 is commonly an order of magnitude smaller than K_1 and K_3 for rodlike suspensions [2].

In the “one-constant approximation,” the constants in Eq. (1) are all assumed to be equivalent to a single constant K , and the energy density may be written as $\mathcal{F} = (K/2)\partial_i n_j \partial_i n_j = (K/2)\|\nabla \mathbf{n}\|^2$ (here and elsewhere, matrix and tensor norms are taken to be the Frobenius norm). In two-dimensional systems, the director field may be written in terms of an angle field $\theta(\mathbf{x})$ such that $\mathbf{n} = (\cos \theta, \sin \theta, 0)$, the one-constant approximation then takes a yet simpler form, $\mathcal{F} = (K/2)|\nabla \theta|^2$. One natural setting in which this two-dimensional representation emerges is in smectic films, where the LC molecules are positionally ordered along one direction (in contrast to a nematic phase, which lacks positional order) [47–49]. A nematic LC may also be confined in the third dimension, allowing the fluid to only deform in-plane [50,51], or be truly two dimensional and one molecule thick, as is the case in Langmuir monolayers [52–54]. Varying the director field in a manner that changes the energy results in fluid stresses (see Sec. II A).

In settings where disclination (line) defects are present, the Oseen-Frank energy density in Eq. (1) is strongly singular (the integrated energy is infinite). This issue has been accounted for by various means, including the excision of a small region local to a line defect and replacing the energy there with a finite core energy. A regularized core energy then accounts for the true energy, which must involve a local “melting” of orientational order [55]. Another approach has been to use an energy like that in Eq. (1), but with a soft penalty that allows $|\mathbf{n}|$ to drop below unity—a regularization inspired by Ginzburg-Landau theory [56,57].

The most common approach, however, is to construct a theory on a higher moment of the orientational distribution, namely the “ \mathbf{Q} tensor.” For a uniaxial LC, the \mathbf{Q} tensor is defined as $\mathbf{Q} = S(\mathbf{nn} - \mathbf{I}/3)$, where \mathbf{nn} is a dyadic product, \mathbf{I} is the identity matrix, and S is a spatially varying scalar-order parameter that indicates the degree to which the LC is in local alignment (the temperature-dependent Maier-Saupe order parameter) [2,58,59]. The principle eigenvector of the symmetric, traceless matrix \mathbf{Q} is the mean orientation, \mathbf{n} . The free energy associated with \mathbf{Q} is decomposed into long-range (elastic) and short-range energies, $\mathcal{F} = \mathcal{F}_E + \mathcal{F}_S$, which we introduce in turn.

The long-range energy density, \mathcal{F}_E , is the Landau–de Gennes energy density, which combines rotationally invariant terms that are quadratic in $\nabla\mathbf{Q}$. For a uniaxial system,

$$\begin{aligned} \mathcal{F}_E(\mathbf{Q}, \nabla\mathbf{Q}) &= \frac{L_1}{2} Q_{ij,k} Q_{ij,k} + \frac{L_2}{2} Q_{ij,j} Q_{ik,k} + \frac{L_3}{2} Q_{ij,k} Q_{ik,j} + \frac{L_4}{2} Q_{mn} Q_{ij,m} Q_{ij,n} \\ &= \frac{L_1}{2} \|\nabla\mathbf{Q}\|^2 + \frac{L_2}{2} |\nabla \cdot \mathbf{Q}|^2 + \frac{L_3}{2} \nabla\mathbf{Q} : (\nabla\mathbf{Q})^T + \frac{L_4}{2} \mathbf{Q} : [\nabla\mathbf{Q} : (\nabla\mathbf{Q})^T], \end{aligned} \quad (2)$$

where repeated indices imply summation, indices after commas indicate partial derivatives, and the third-order transpose is defined such that $(\mathbf{A}^T)_{ijk} = \mathbf{A}_{kji}$. The third term, with coefficient L_3 , is often omitted since it can be related to the second term using $Q_{ij,k} Q_{ik,j} = Q_{ij,j} Q_{ik,k} + (Q_{ij} Q_{ik,j} - Q_{ik} Q_{ij,j})_{,j}$ and integrating by parts. In addition, the single cubic term with coefficient L_4 is not exhaustive but is included in service of stability [60]. The Oseen-Frank energy, Eq. (1), is reproduced if S is fixed, and $L_1 = (3K_2 - K_1 + K_3)/(6S^2)$, $L_2 = (K_1 - K_{24})/S^2$, $L_3 = (K_{24} - K_2)/S^2$, and $L_4 = (K_3 - K_1)/(2S^3)$. In the one-constant approximation only L_1 is nonzero, and $\mathcal{F}_E = (L_1/2) \|\nabla\mathbf{Q}\|^2$. As in the Oseen-Frank theory, relations between these constants are necessary to ensure stability [44,61,62]. An intermediate theory which takes \mathbf{n} and S as order parameters results in the Ericksen model [63].

The short-range energy density, \mathcal{F}_S , commonly called the bulk or thermodynamic energy density, is due to near-field interactions among molecules, including steric and electrostatic effects. It is commonly modeled by a truncated Landau–de Gennes expansion (an expansion in S near the isotropic-nematic phase transition), most commonly in the form (using $S^2 = 3\text{Tr}(\mathbf{Q}^2)/2$):

$$\begin{aligned} \mathcal{F}_S(\mathbf{Q}) &= \frac{A}{2} \left(1 - \frac{U}{3}\right) Q_{ij} Q_{ji} - \frac{AU}{3} Q_{ij} Q_{jk} Q_{ki} + \frac{AU}{4} (Q_{ij} Q_{ji})^2 \\ &= \frac{A}{2} \left(1 - \frac{U}{3}\right) \text{Tr}(\mathbf{Q}^2) - \frac{AU}{3} \text{Tr}(\mathbf{Q}^3) + \frac{AU}{4} \text{Tr}(\mathbf{Q}^2)^2, \end{aligned} \quad (3)$$

with A an energy scale for the phase transition and U the “nematic strength.” The scalar-order parameter is given approximately by $S \approx 1/4 + (3/4)[1 - 8/(3U)]^{1/2}$ and the system is in the nematic phase when $U \geq 2.8$ [64–66]. The general form of the fourth-order expansion was derived in Ref. [67]. See Ref. [64] for a first-principles development from the distributional perspective, and Ref. [68] and Sec. V for a survey of numerical methods for their study.

II. RIGID BODIES AND BOUNDARIES

When a boundary is introduced to a liquid crystal, whether as an outer confining boundary or as an immersed body, surface anchoring physics tends to play an outsized role. Anchoring conditions

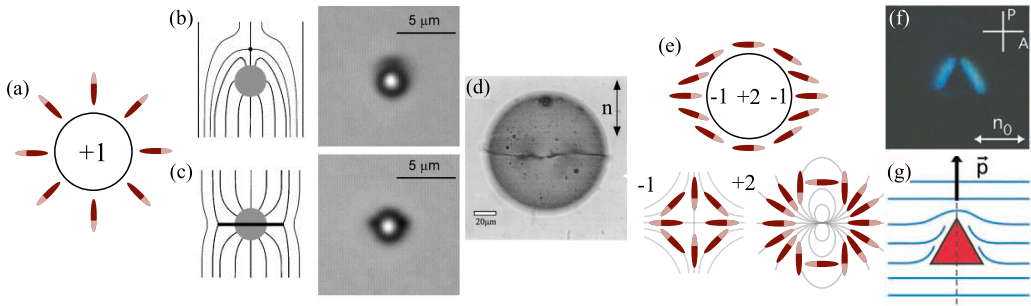


FIG. 2. (a) Homeotropic (normal) anchoring on the surface of a sphere corresponds to a $+1$ topological charge. Molecular orientation is indicated by color. (b) Topological balance is achieved in a dipolar LC configuration; or (c) a (quadrupolar) “Saturn-ring” configuration. The background director field is vertical in both cases. Reproduced from Ref. [70]. (d) A Saturn-ring defect around a large ($100\ \mu\text{m}$ diameter) particle. Reproduced from Ref. [71]. (e) The LC configuration with planar anchoring on a cylindrical boundary may be represented as two virtual -1 topological defects and one $+2$ defect in the interior of the cylinder. The molecular orientation is colored to show the degree of reorientation. [(f) and (g)] A triangular particle in a nematic LC (horizontal director in the far field) with tangential anchoring deforms the LC, as viewed (top) under cross-polarized lenses. Reproduced from Ref. [72].

for the LC at the boundary account for a chemically or mechanically preferred relative orientation; common situations produce homeotropic (normal) and homogeneous (planar) anchoring conditions of a given energetic strength. The fact that boundary conditions can so completely tune the bulk configuration (as well as susceptibility to electric and magnetic fields) underlies many of the familiar LC commercial applications [69].

Internal boundaries (e.g., those introduced by immersed bodies) present a rich array of possibilities. In addition to imposing boundary conditions on the LC, they are also mobile, responding to the background director field and to each other. Liquid crystal configurations around rigid particles have been explored experimentally, numerically, and analytically by a wealth of authors, with notable reviews given by Stark [73], Muševič [74,75], and Smalyukh [76]. Even a single colloid’s interaction with a nonuniform background director field is nontrivial, and offers a pathway towards “levitation” and transport [77,78].

Not only does the LC field need to deform to accommodate these offending boundaries, but topological invariance can force defects to appear elsewhere in the fluid. A standard example is that of a sphere with strong (infinite-strength) homeotropic (normal) anchoring conditions, corresponding to a $+1$ “hedgehog” topological defect, as shown in Fig. 2(a). If the director field is uniform in the far-field, then this $+1$ “topological charge” must be canceled somewhere in the bulk fluid; this can take the form of a single -1 point defect [the dipolar configuration, Fig. 2(b)] or a quadrupolar “Saturn-ring” defect, appearing as two $-1/2$ defects when viewed in a cross section [Fig. 2(c)] [70,79–81]. Figure 2(d) shows a closer view of a Saturn-ring defect around a large ($100\ \mu\text{m}$) particle [71]; as in Fig. 2(c), the background director field is vertical (in the direction of the double arrow). More exotic possibilities arise in cholesteric LCs [82].

Tangential (homogeneous) anchoring may instead introduce “boojum” -1 defects at the particle surface [83]. The LC director field external to a cylinder may be represented as two virtual -1 topological defects and one $+2$ defect in the interior of the cylinder [see Fig. 2(e)] [84]. This quadrupolar structure is generic for widely separated particles with planar anchoring conditions, though short-range interactions may become dominant due to bifurcations in topological defect positioning on the particle surface [85], resulting in transitions from repulsive to attractive interactions of bodies. Particle shape naturally affects the equilibrium LC configuration as well. Figures 2(f) and 2(g) show the LC distortion around a triangular particle with tangential anchoring conditions,

viewed through cross-polarized lenses [72]. The topological defects tend to position themselves at or near sharp corners on such a body, reminiscent of the Kutta condition in classical potential flow [84].

Hedgehog, Saturn-ring, and dipolar configurations are axisymmetric and twist free. But the energy-minimizing LC configuration can include such a twist (similar to a swirl flow in fluid mechanics) for a sufficiently small twist elastic constant relative to the bend and splay constants. The criterion for twist relaxation to appear in the energy-minimizing configuration around a sphere, $K_2/K_1 < 2.32(1 - K_3/K_1)$, is known as the Williams condition [86–88].

A. Equilibrium and anchoring boundary conditions

Confining or immersed boundaries introduce an additional energetic penalty to deviations from a preferred orientation, which may be spatially varying along a surface. This energetic penalty is typically described by a surface energy density (energy per unit area), \mathcal{F}_s . The total system energy, \mathcal{E} , combines the bulk LC elasticity with this surface “anchoring” energy,

$$\mathcal{E} = \int_{\Omega} \mathcal{F} dV + \int_{\partial\Omega} \mathcal{F}_s dA, \quad (4)$$

where Ω denotes the fluid domain and $\partial\Omega$ its boundary (including internal body surfaces), dV and dA are infinitesimal volume and surface area elements, and \mathcal{F} is modeled either by Eq. (1) or Eqs. (2) and (3). The director field at equilibrium minimizes the total system energy above.

In the theory based on the director field \mathbf{n} , first carried out by Ericksen [89], the surface energy can be written as $\mathcal{F}_s(\mathbf{n}; \mathbf{v}, \boldsymbol{\tau})$, where \mathbf{v} is the unit normal vector pointing into the LC and $\boldsymbol{\tau}$ is a special unit tangent vector of the surface. As an example, in the Rapini-Papoular model [90,91], the anchoring energy is assumed to be locally quadratic in the deviation away from a preferred orientation $\mathbf{n}_0 = (\mathbf{n}_0 \cdot \mathbf{v})\mathbf{v} + (\mathbf{n}_0 \cdot \boldsymbol{\tau})\boldsymbol{\tau}$, while respecting the $\mathbf{n} \mapsto -\mathbf{n}$ symmetry of the rodlike molecules:

$$\mathcal{F}_s = \frac{W}{2}(1 - (\mathbf{n} \cdot \mathbf{n}_0)^2), \quad (5)$$

where W is the anchoring strength (with units of energy per unit area). Degenerate planar anchoring, in which the molecules may rotate in the tangent plane of the surface with no energetic cost, can similarly be imposed through an energy density

$$\mathcal{F}_s = \frac{W}{2}(\mathbf{n} \cdot \mathbf{v})^2. \quad (6)$$

Changes in the bulk LC energy due to variations in the \mathbf{n} field (denoted by $\delta\mathbf{n}$) are measured by the functional derivative of \mathcal{E} :

$$\delta\mathcal{E} = \int_{\Omega} \frac{\partial\mathcal{F}}{\partial\mathbf{n}} \cdot \delta\mathbf{n} + \frac{\partial\mathcal{F}}{\partial\nabla\mathbf{n}} : \nabla(\delta\mathbf{n}) - \lambda\mathbf{n} \cdot \delta\mathbf{n} dV + \int_{\partial\Omega} \frac{\partial\mathcal{F}_s}{\partial\mathbf{n}} \cdot \delta\mathbf{n} - \mu\mathbf{n} \cdot \delta\mathbf{n} dA, \quad (7)$$

where λ and μ are Lagrange multipliers imposing $|\mathbf{n}| = 1$ [92]. For two matrices \mathbf{A} and \mathbf{B} , we define $\mathbf{A} : \mathbf{B} = \text{Tr}(\mathbf{A}^T \mathbf{B}) = A_{ij}B_{ij}$, the Frobenius inner product. Integrating by parts yields

$$\delta\mathcal{E} = - \int_{\Omega} (\mathbf{h} + \lambda\mathbf{n}) \cdot \delta\mathbf{n} dV - \int_{\partial\Omega} (\mathbf{h}_s + \mu\mathbf{n}) \cdot \delta\mathbf{n} dA, \quad (8)$$

where we have introduced the bulk and surface molecular fields

$$\mathbf{h} = \nabla \cdot \boldsymbol{\Pi} - \frac{\partial\mathcal{F}}{\partial\mathbf{n}} \quad \text{and} \quad \mathbf{h}_s = \mathbf{v} \cdot \boldsymbol{\Pi} - \frac{\partial\mathcal{F}_s}{\partial\mathbf{n}}, \quad (9a,b)$$

respectively, with $\boldsymbol{\Pi} = \partial\mathcal{F}/\partial\nabla\mathbf{n}$ the Ericksen torque stress tensor. At an energy-minimizing equilibrium, $\delta\mathcal{E} = 0$, in the absence of any external field we must have $\mathbf{h} = -\lambda\mathbf{n}$. Hence, the component

of \mathbf{h} that is orthogonal to \mathbf{n} is everywhere zero, i.e.,

$$[\mathbf{h}]^\perp := \mathbf{P}(\mathbf{n}) \cdot \mathbf{h} = \mathbf{0} \quad \text{in } \Omega, \quad (10)$$

for the projection operator $\mathbf{P}(\mathbf{n}) = \mathbf{I} - \mathbf{n}\mathbf{n}$. In the special case of the one-constant approximation, where $\mathcal{F} = (K/2)\|\nabla\mathbf{n}\|^2$, we have $\mathbf{\Pi} = K\nabla\mathbf{n}$ and $\mathbf{h} = K\nabla^2\mathbf{n}$, and in two dimensions we simply have that the director angle field is harmonic, $\nabla^2\theta = 0$. See Appendix A 1 and Refs. [2,46,93] for more complete discussions.

Natural boundary conditions are also apparent. Since we must have $\mathbf{h}_s = -\mu\mathbf{n}$ at equilibrium, the component of \mathbf{h}_s that is orthogonal to \mathbf{n} must also vanish, i.e.,

$$[\mathbf{h}_s]^\perp = \mathbf{0} \quad \text{on } \partial\Omega. \quad (11)$$

For instance, using the Rapini-Papoular model in Eq. (5) with the one-constant approximation, we find Robin boundary conditions for the equilibrium director field, with $\mathbf{h}_s = K(\mathbf{v} \cdot \nabla\mathbf{n}) + W(\mathbf{n} \cdot \mathbf{n}_0)\mathbf{n}_0$. Furthermore, in two dimensions, the boundary condition reduces to $K(\mathbf{v} \cdot \nabla\theta) = (W/2)\sin[2(\theta - \theta_0)]$, where θ_0 is the preferred director angle, i.e., $\mathbf{n}_0 = (\cos\theta_0, \sin\theta_0, 0)$, which may be spatially varying.

The quantity K/W is called the extrapolation length, it is the distance into the interior of an infinite, flat boundary at which the strong (infinite) anchoring conditions could instead be applied with the same resulting director field everywhere [2]. Surface curvature makes this concept only approximate, as discussed in Ref. [84]. In addition, given a length scale a (perhaps associated with an immersed body), a dimensionless anchoring strength, $w = aW/K$, indicates the extent to which the boundary condition is dictated by the bulk energy (Neumann condition) or the surface energy (Dirichlet condition).

Although dynamics are outside the scope of this review, Ericksen-Leslie theory accounts for viscous relaxation of the director field, both through molecular reorientation and through a bulk flow [94]. The rotational viscosity, γ , sets a timescale for relaxation by the evolution of the director field. If the rotational viscosity is small, director rotation dominates other mechanisms of energy relaxation (in particular, flow), and the director field dynamics are governed approximately by $\partial\mathbf{n}/\partial t = [\mathbf{h}]^\perp/\gamma$, also known as Ginzburg-Landau relaxation. In two dimensions with the one-constant approximation, this results in a heat equation for the angle field, $\partial\theta/\partial t = (K/\gamma)\nabla^2\theta$.

A similar calculation is carried out when instead using the Landau-de Gennes theory based on the \mathbf{Q} tensor. Here the functional derivative of \mathcal{E} is

$$\delta\mathcal{E} = \int_{\Omega} \frac{\partial\mathcal{F}}{\partial\mathbf{Q}} : \delta\mathbf{Q} + \frac{\partial\mathcal{F}}{\partial\nabla\mathbf{Q}} : \nabla(\delta\mathbf{Q}) - \mathbf{\Lambda} : \delta\mathbf{Q} dV + \int_{\partial\Omega} \frac{\partial\mathcal{F}_s}{\partial\mathbf{Q}} : \delta\mathbf{Q} - \boldsymbol{\mu} : \delta\mathbf{Q} dA, \quad (12)$$

with $\Lambda_{ij} = \lambda\delta_{ij} + \lambda_k\epsilon_{ijk}$ and $\mu_{ij} = \mu\delta_{ij} + \mu_k\epsilon_{ijk}$, where δ_{ij} and ϵ_{ijk} are the components of the Kronecker delta and Levi-Civita tensor, respectively, and λ , λ_k , μ , and μ_k are Lagrange multipliers that impose the symmetries $\text{Tr}(\mathbf{Q}) = 0$ and $\mathbf{Q}^T = \mathbf{Q}$. Integrating by parts yields

$$\delta\mathcal{E} = - \int_{\Omega} (\mathbf{H} + \mathbf{\Lambda}) : \delta\mathbf{Q} dV - \int_{\partial\Omega} (\mathbf{H}_s + \boldsymbol{\mu}) : \delta\mathbf{Q} dA, \quad (13)$$

where we have introduced the bulk and surface molecular fields (which are now second-order tensors)

$$\mathbf{H} = \nabla \cdot \mathbf{\Pi} - \frac{\partial\mathcal{F}}{\partial\mathbf{Q}} \quad \text{and} \quad \mathbf{H}_s = \mathbf{v} \cdot \mathbf{\Pi} - \frac{\partial\mathcal{F}_s}{\partial\mathbf{Q}}, \quad (14a,b)$$

respectively, with $\mathbf{\Pi} = \partial\mathcal{F}/\partial\nabla\mathbf{Q}$ now a third-order tensor. Absent any external fields, energy minimization is achieved when $\mathbf{H} = -\mathbf{\Lambda}$, and the analog of Eq. (10) is that the symmetric and traceless (ST) part of the molecular field vanishes at equilibrium,

$$[\mathbf{H}]^{ST} := \frac{1}{2}(\mathbf{H} + \mathbf{H}^T) - \frac{1}{3}\text{Tr}(\mathbf{H})\mathbf{I} = \mathbf{0} \quad \text{in } \Omega. \quad (15)$$

The natural boundary conditions in this setting are given by $\mathbf{H}_s = -\boldsymbol{\mu}$; that is, the analog to Eq. (11) is

$$[\mathbf{H}_s]^{ST} = \mathbf{0} \quad \text{on } \partial\Omega, \quad (16)$$

see Appendix A 1 and Refs. [95,96] for further details.

Surface anchoring energies are carried forth from those used in \mathbf{n} -field theories. The analog of the Rapini-Papoular energy is a surface energy density

$$\mathcal{F}_s = \frac{W}{2} \text{Tr}[(\mathbf{Q} - \mathbf{Q}_0)^2], \quad (17)$$

where W is the anchoring strength and $\mathbf{Q}_0 = S_0(\mathbf{n}_0\mathbf{n}_0 - \mathbf{I}/3)$, with the preferred direction \mathbf{n}_0 and the corresponding ordering S_0 on the surface [97]. For degenerate planar anchoring, instead the Fournier-Galatola energy is commonly used,

$$\mathcal{F}_s = \frac{W}{2} \text{Tr}[(\bar{\mathbf{Q}} - \bar{\mathbf{Q}}_\perp)^2], \quad (18)$$

where $\bar{\mathbf{Q}} = \mathbf{Q} + (S/3)\mathbf{I}$ and $\bar{\mathbf{Q}}_\perp = \mathbf{P}(\mathbf{v}) \cdot \bar{\mathbf{Q}} \cdot \mathbf{P}(\mathbf{v})$, with $\mathbf{P}(\mathbf{v}) = \mathbf{I} - \mathbf{v}\mathbf{v}$ the surface projection operator [98]. For example, in the one-constant approximation, where $\mathcal{F} = (L_1/2)\|\nabla\mathbf{Q}\|^2 + \mathcal{F}_s(\mathbf{Q})$ with \mathcal{F}_s given in Eq. (3), we have $\boldsymbol{\Pi} = L_1\nabla\mathbf{Q}$ and $\mathbf{H} = L_1\nabla^2\mathbf{Q} - \partial\mathcal{F}_s/\partial\mathbf{Q}$. Additionally, with the Rapini-Papoular surface energy in Eq. (17), we have $\mathbf{H}_s = L_1\mathbf{v} \cdot \nabla\mathbf{Q} - W(\mathbf{Q} - \mathbf{Q}_0)$.

Models of \mathbf{Q} field evolution include Doi-Onsager molecular theories [58,64,99,100] and the Beris-Edwards model [65] (which has been shown to be equivalent to the Ericksen-Leslie theory in a particular limit [100,101]). As before, in the simplest setting of a small rotational viscosity, which provides a separation of timescales between director-field relaxation and fluid flow, the \mathbf{Q} tensor evolves according to the Ginzburg-Landau relaxation, $\partial\mathbf{Q}/\partial t = [\mathbf{H}]^{ST}/\gamma$.

B. Body forces, torques, and traction

In order to predict the force and torque (as well as the pointwise tractions and moments) of the LC on a confining or immersed boundary, we must return to the equations governing the equilibrium LC configuration. In the presentation of Sec. II A, natural boundary conditions emerged simply when considering variations in \mathbf{n} or \mathbf{Q} . We neglected there, however, another generic means of elastic energy relaxation: spatial repositioning of molecules.

Starting again with the theory constructed on the director field \mathbf{n} , a more complete variational principle involves varying both the LC's material position, $\delta\mathbf{x}$, and the director field, $\delta\mathbf{n}$. By the principle of virtual work, we have

$$\delta\mathcal{E} = - \int_{\Omega} \mathbf{F} \cdot \delta\mathbf{x} + \mathbf{G} \cdot \Delta\mathbf{n} dV - \int_{\partial\Omega} \mathbf{f} \cdot \delta\mathbf{x} + \mathbf{g} \cdot \Delta\mathbf{n} dA, \quad (19)$$

where we have introduced the Eulerian variation $\Delta\mathbf{n} = \delta\mathbf{n} + \delta\mathbf{x} \cdot \nabla\mathbf{n}$, force (per unit volume) acting on the bulk \mathbf{F} , force (per unit area) acting on the boundary \mathbf{f} , generalized force (per unit volume) acting on the bulk \mathbf{G} , and generalized force (per unit area) acting on the boundary \mathbf{g} . These generalized forces are related to the couple vectors acting on the bulk and the boundary according to $\mathbf{M} = \mathbf{n} \times \mathbf{G}$ and $\mathbf{m} = \mathbf{n} \times \mathbf{g}$, respectively [2,93].

For bulk and surface energy densities with functional dependence $\mathcal{F}(\mathbf{n}, \nabla\mathbf{n})$ and $\mathcal{F}_s(\mathbf{n}; \mathbf{v}, \boldsymbol{\tau})$, calculus of variations leads to expressions for these forces and couples (see Appendix A 1 and Refs. [2,46,93,102]), that is,

$$\mathbf{F} = \nabla \cdot \mathbf{T}, \quad \mathbf{f} = \mathbf{v} \cdot \mathbf{T} + \nabla_s \cdot \mathbf{T}_s, \quad \mathbf{M} = \mathbf{n} \times \mathbf{h}, \quad \mathbf{m} = \mathbf{n} \times \mathbf{h}_s, \quad (20a-d)$$

using the surface divergence $\nabla_s = \mathbf{P}(\mathbf{v}) \cdot \nabla$; bulk and surface molecular fields, \mathbf{h} and \mathbf{h}_s , defined in Eq. (9); and the bulk and surface stress tensors,

$$\mathbf{T} = -p\mathbf{I} - \boldsymbol{\Pi} \cdot \nabla\mathbf{n}^T \quad \text{and} \quad \mathbf{T}_s = \mathcal{F}_s\mathbf{P}(\mathbf{v}) - \mathbf{P}(\mathbf{v}) \cdot \frac{\partial\mathcal{F}_s}{\partial\mathbf{v}}\mathbf{v} + \boldsymbol{\tau} \frac{\partial\mathcal{F}_s}{\partial\boldsymbol{\tau}} \cdot \mathbf{P}(\boldsymbol{\tau}), \quad (21a,b)$$

where p is an unknown pressure and $\mathbf{\Pi} = \partial\mathcal{F}/\partial\nabla\mathbf{n}$ is the Ericksen torque stress tensor. The tensor \mathbf{T} is called the Ericksen stress tensor and describes the elastic stresses inside the LC. The tensor \mathbf{T}_s provides an additional source of stress on any confining or immersed boundaries. Such additional sources of stress arise when incorporating other functional dependencies in the energy densities \mathcal{F} and \mathcal{F}_s . For example, including a spatial dependence in the surface energy (e.g., a spatially varying anchoring strength, W) leads to an additional Marangoni-like stress $\mathbf{f} = -\partial\mathcal{F}_s/\partial\mathbf{x}$ (see Ref. [102], for example).

In the absence of any external fields, the equilibrium equations, Eq. (10) subject to Eq. (11), require that the moments in Eqs. (20c) and (20d) vanish, i.e., $\mathbf{M} = \mathbf{m} = \mathbf{0}$. Additionally, imposing $\mathbf{F} = \mathbf{0}$ in Eq. (20a) yields the pressure up to an additive constant, $p = -\mathcal{F}$. This leaves the surface force equation, Eq. (20b), which provides an expression for the traction acting on a boundary. As an example, $\mathbf{\Pi} = K\nabla\mathbf{n}$ in the one-constant approximation, and so

$$\mathbf{T} = \frac{K}{2} \|\nabla\mathbf{n}\|^2 \mathbf{I} - K\nabla\mathbf{n} \cdot \nabla\mathbf{n}^T, \quad (22)$$

using the Frobenius norm. Furthermore, the Rapini-Papoular model in Eq. (5) yields the additional surface stress,

$$\mathbf{T}_s = \frac{W}{2} (1 - (\mathbf{n} \cdot \mathbf{n}_0)^2) \mathbf{P}(\mathbf{v}) + W(\mathbf{n} \cdot \mathbf{n}_0) \mathbf{P}(\mathbf{v}) \cdot (\mathbf{nn}_0 - \mathbf{n}_0\mathbf{n}) \cdot \mathbf{P}(\boldsymbol{\tau}), \quad (23)$$

for the relaxed direction $\mathbf{n}_0 = (\mathbf{n}_0 \cdot \boldsymbol{\tau})\boldsymbol{\tau} + (\mathbf{n}_0 \cdot \mathbf{v})\mathbf{v}$. As $W \rightarrow \infty$, strong (infinite) anchoring is recovered from Eq. (11), i.e., $\mathbf{n} \sim \mathbf{n}_0$ on ∂D , and the additional stress takes the form $\mathbf{T}_s \sim \mathbf{P}(\mathbf{v}) \cdot [(\mathbf{v} \cdot \mathbf{\Pi})\mathbf{n}_0 - \mathbf{n}_0(\mathbf{v} \cdot \mathbf{\Pi})] \cdot \mathbf{P}(\boldsymbol{\tau})$. In two dimensions, these tensors can be written in terms of a director angle, θ , and its preferred boundary value, θ_0 :

$$\mathbf{T} = \frac{K}{2} |\nabla\theta|^2 \mathbf{I} - K\nabla\theta\nabla\theta \quad \text{and} \quad \mathbf{T}_s = \frac{W}{2} \sin^2(\theta - \theta_0) \mathbf{v}^\perp \mathbf{v}^\perp + \frac{W}{2} \sin[2(\theta - \theta_0)] \mathbf{v}^\perp \mathbf{v}, \quad (24a,b)$$

where \mathbf{v}^\perp is \mathbf{v} rotated by 90° counterclockwise. Here the strong anchoring limit, $W \rightarrow \infty$, yields the boundary condition $\theta \sim \theta_0$ on ∂D and the surface stress tensor $\mathbf{T}_s \sim K(\mathbf{v} \cdot \nabla\theta) \mathbf{v}^\perp \mathbf{v}$.

The surface tractions on an immersed cylinder in a two-dimensional LC are shown in Fig. 3(a), where finite-strength ($w = aW/K = 1$, with a the cylinder radius) tangential anchoring conditions have been imposed, and the background director field is horizontal. The director and traction fields are found analytically using methods from complex variables, as briefly discussed in Sec. III. In this case, the LC configuration is given exactly by a single $+2$ topological defect at the cylinder center, and two -1 defects interior to the surface by a distance that depends on the anchoring strength [84]. Looking ahead to the discussion on deformable bodies, the energy stored in LC splay near the fore and aft points on the body would be reduced if the body were to elongate in those directions. The LC bend above and below the cylinder would also be reduced by an increase in the body aspect ratio, assuming the body area is unchanged, resulting in the inward-pointing tractions on those parts of the body surface. For both reasons, we should expect body elongation with these anchoring boundary conditions, a theoretical result that we will see played out in numerous experimental settings below.

Figure 3(b) shows the traction on a Janus particle (normal anchoring conditions on the left half, tangential anchoring on the right half), again with anchoring strength $w = 1$. There is no net force on the cylinder in equilibrium, but here again the expected deformations of a soft particle can be predicted—deformations should inherit the lack of left-right symmetry apparent in the traction field. Finally, Figs. 3(c) and 3(d) show two examples with homeotropic (normal) anchoring conditions with large, but finite, anchoring strength ($w = 100$). Their $+1$ topological charges are balanced by defects in the bulk LC, in two-dimensional versions of the dipolar configuration [e.g., Fig. 2(b)], and in Saturn-ring configuration [e.g., Fig. 2(c)]. As we will see again shortly, even though both experience zero net force at equilibrium, deformations in the direction of the defects appear as natural means of reducing stored LC bulk elastic energy and presenting the surface to the LC in such a way as to more immediately satisfy the preferred anchoring conditions.

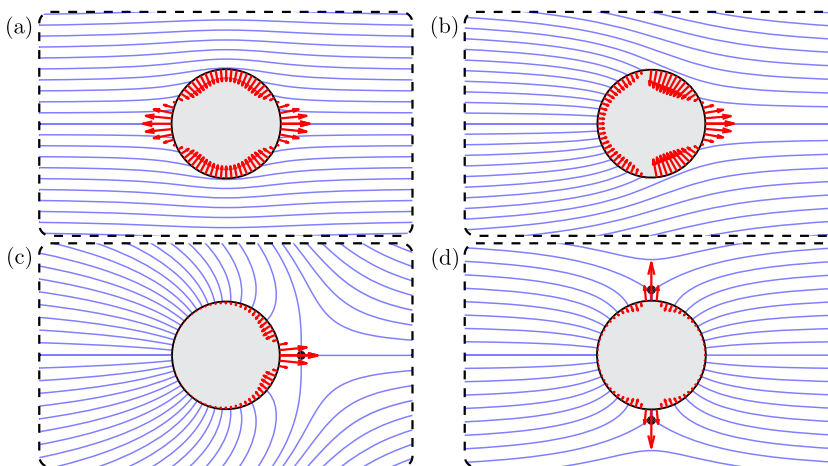


FIG. 3. Surface traction fields on a cylinder of radius a with: (a) tangential anchoring conditions and anchoring strength $w = aW/K = 1$; (b) Janus boundary conditions (normal anchoring on the left half, tangential anchoring on the right half) and again $w = aW/K = 1$; (c) homeotropic (normal) anchoring conditions with an exterior -1 topological defect and $w = aW/K = 100$, a two-dimensional version of the dipole configuration in Fig. 2(b); (d) homeotropic anchoring conditions with two exterior $-1/2$ topological defects and $w = aW/K = 100$, a two-dimensional version of the Saturn-ring configuration in Fig. 2(c).

Similar stress tensors may be derived for theories based on the \mathbf{Q} tensor; see Appendix A 2 and Refs. [40,95], for example. For the energy densities of the form $\mathcal{F}(\mathbf{Q}, \nabla\mathbf{Q})$ and $\mathcal{F}_s(\mathbf{Q}; \mathbf{v}, \boldsymbol{\tau})$, the body and surface forces, \mathbf{F} and \mathbf{f} , are again given by Eqs. (20a) and (20b), with the surface stress tensor, \mathbf{T}_s , given by Eq. (21b) and bulk stress tensor now defined as

$$\mathbf{T} = -p\mathbf{I} - \boldsymbol{\Pi} : (\nabla\mathbf{Q})^T, \quad (25)$$

for $\boldsymbol{\Pi} = \partial\mathcal{F}/\partial\nabla\mathbf{Q}$. In the absence of external forcing, the pressure here is again given by the energy density up to an additive constant, $p = -\mathcal{F}$. For instance, $\boldsymbol{\Pi} = L_1\nabla\mathbf{Q}$ in the one-constant approximation, which yields

$$\mathbf{T} = \frac{L_1}{2}\|\nabla\mathbf{Q}\|^2\mathbf{I} - L_1\nabla\mathbf{Q} : (\nabla\mathbf{Q})^T, \quad (26)$$

again using the tensor Frobenius norm. Furthermore, the i th component of the couple vectors acting on the bulk and the boundary are

$$M_i = \epsilon_{ijk}(\mathbf{Q} \cdot \mathbf{H} - \mathbf{H} \cdot \mathbf{Q})_{jk} \quad \text{and} \quad m_i = \epsilon_{ijk}(\mathbf{Q} \cdot \mathbf{H}_s - \mathbf{H}_s \cdot \mathbf{Q})_{jk}, \quad (27a,b)$$

respectively, where repeated indices indicate summation and \mathbf{H} and \mathbf{H}_s are the molecular field tensors defined in Eq. (14). Note that both these couple vectors vanish at equilibrium with no external body or surface moments, Sec. II A.

III. MULTIPLE RIGID BODIES

When multiple colloidal bodies are introduced to an elastic environment, their quasistatic interactions are dictated by the elastic energy stored in the medium. Just as multiple droplets on a soft substrate move to reduce an elastic energy [103–106] and floating particles move to reduce the interfacial surface energy [107–109], so, too, can particles immersed in an LC move to reduce the bulk elastic energy. Complex near-body interactions may also emerge due to the positional rearrangement of essential topological defects [70,110–112]. Spherical colloids with the dipolar LC structure of Fig. 2(b) can align in the direction of the background director field [Fig. 4(a)] or if in the

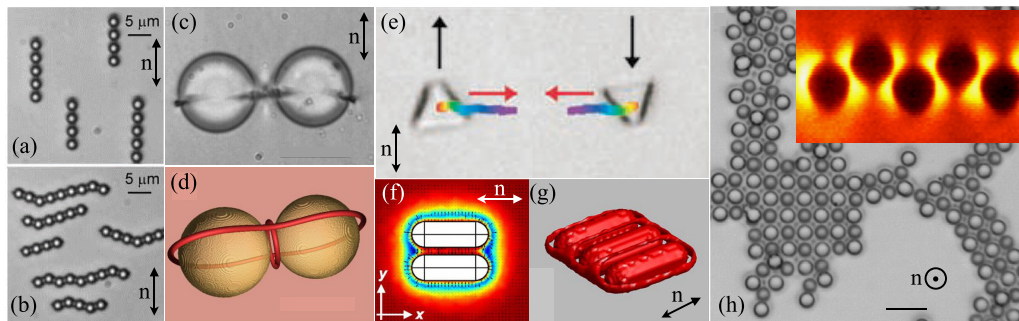


FIG. 4. [(a) and (b)] The dipolar defect configuration of Fig. 2(b) can result in director-aligned multicolloid chaining, while the Saturn-ring (quadrupolar) configuration of Fig. 2(c) leads to side-by-side chaining. The background director field is indicated by a double arrow. Reproduced from Ref. [70]. [(c) and (d)] Saturn-ring defects around two spheres of diameter $19\ \mu\text{m}$ merge into an “entangled hyperbolic defect,” in experiments and simulations. Reproduced from Ref. [124]. (e) Interactions can depend on particle orientation; two triangular particles in anti-alignment, in a vertical background director field, attract. Reproduced from Ref. [72]. (f) Two elongated particles settle into an energy-minimizing lateral configuration; the field is colored by the scalar order parameter S , showing greater disorder (melting and defects) close to the bodies. Reproduced from Ref. [126]. (g) Three elongated particles, with a complex “defect” (isosurfaces of $S = 0.25$ are shown). Reproduced from Ref. [126]. (h) Multiple colloids with dipolar defects exhibit “antiferromagnetic” defect placement (alternating orientation among neighbors) in three dimensions; associated out-of-plane displacements are visible with a side-view (inset). Reproduced from Ref. [127].

quadrupolar, Saturn-ring state, align in kinked chains nearly orthogonal to the background director field [Fig. 4(b)] [70]. Spherical colloids with tangential anchoring, meanwhile, are known to form kinked chains aligned at 30° to the LC-preferred alignment axis [85,113–117] or more complex crystal lattice structures [118,119].

The defects produced by interacting colloids can be deformed more substantially [59,120–122], leading to beautiful, entangled defect loops [123]. Figures 4(c) and 4(d) show two spherical colloids whose Saturn-ring defects have merged into a single “entangled hyperbolic defect” [124] (or “figure of theta defect” [50]); see also Refs. [122,125], and the review by Tkalec and Muševič [50].

Colloid interactions can also be tuned by both the particle shape and orientation. Lapointe *et al.* [72] examined regular polygons immersed in a nematic LC [shown in Figs. 2(f) and 2(g)], and found that attraction or repulsion can be set by the relative particle orientations, as shown in Fig. 4(e). Red arrows indicate the direction of forcing on each body. The interaction of elongated bodies in a LC is strongly influenced not only by their anchoring boundary conditions but also by their aspect ratio [128,129]. Elongated bodies can also lead to a number of different chain configurations [130]. Figure 4(f) shows two such particles, which settle into an energy-minimizing lateral configuration relative to the background director field; Fig. 4(g) shows a similar result for three particles, with a complex “defect” shown (isosurfaces of $S = 0.25$) [126]. A broader review of colloidal chains may be found in Ref. [131]. More recent work has seen more intricate patterns, for instance fractal colloidal self-assembly [132]. Confining boundaries can add an extra layer of complexity to these interactions [133,134].

Ongoing work on the interactions of rigid particles include examination of different LC phases, like chiral magnetic and cholesteric LCs [135], and three-dimensional self-assembly which, like chaining, is governed by topological defect positioning [127]. Recent observed phenomena include “antiferromagnetic” ordering of spheres with alternating dipolar defect structure in three

dimensions, shown in Fig. 4(h). We direct the interested reader to a more substantial overview of colloidal interactions in LCs by Smalyukh [76].

A. Multipole expansion and complex variables techniques

Particle interactions through the LC medium are in general highly nonlinear and depend on the intricate configurations of topological defects produced by the presence of each body in the fluid. Important mathematical insight, however, is offered when it can be assumed that the director field does not substantially deviate from uniformity (even with bodies present) and under the one-constant approximation. Writing $\mathbf{n} = \hat{\mathbf{z}} + \mathbf{n}'$, where $\hat{\mathbf{z}}$ is the unit vector in the direction of the background field and \mathbf{n}' is a small perturbation, which is perpendicular to $\hat{\mathbf{z}}$ since $1 = |\mathbf{n}| \sim 1 + \mathbf{n}' \cdot \hat{\mathbf{z}}$, the equilibrium field must be harmonic, $\mathbf{P}(\mathbf{n}) \cdot \nabla^2 \mathbf{n} \sim \nabla^2 \mathbf{n}' = 0$ (see Sec. II A). The disturbance field due to a particle may then be understood through a classical multipole expansion, just as in electrostatics or hydrodynamics, with coefficients, $\mathbf{a}_{\ell m}$, determined by the anchoring boundary conditions:

$$\mathbf{n}' = \sum_{\ell=0}^{\infty} \sum_{m=-\ell}^{\ell} \mathbf{a}_{\ell m} |\mathbf{x}|^{-\ell-1} Y_{\ell}^m(\eta, \xi), \quad (28)$$

where Y_{ℓ}^m is the spherical harmonic function of degree ℓ and order m and (η, ξ) are angular spherical coordinates. As a simple example, for a spherical particle of radius a , on which nondegenerate planar anchoring to a preferred orientation $\boldsymbol{\tau}$ is assumed, the disturbance caused by the particle is $\mathbf{n}' = (1 + 1/w)^{-1} (a/|\mathbf{x}|) \boldsymbol{\tau}$, with $w = aW/K$ the dimensionless anchoring strength. This disturbance, a monopole, results in a net torque on the body (and an equal and opposite torque on the surrounding LC). Normal or tangential anchoring conditions on torque-free particles are known to give rise to dipolar or quadrupolar far-field interactions, respectively [75, 136–139], with some examples having already been discussed above. More complex surface chemistry can result in yet higher spatial moments [140].

Particle interactions may, in turn, be approximated through a standard method of reflections, leading to the prediction of multipolar interactions in three dimensions [76, 116, 141–144]. Theoretical far-field predictions of interparticle forces, for example those of Ref. [34], have been found to very accurately describe experimental measurements [145]. The one-constant approximation was also found to be accurate in the context of particle interactions in Ref. [146] if the elastic constants are comparable. For systems with much larger elastic penalties to splaying than bending, however, the angle between a chain of quadrupolar particles and the bulk director field was found to be close to 0, in contrast to the typically observed 30°. Furthermore, large differences in elastic constants were found to break the isotropy of interacting asymmetric particles, leading to the possible formation of zones of repulsion, which are not observed under the one-constant approximation.

In two dimensions, recall that the director field may be represented by an angle field $\theta(\mathbf{x})$ such that $\mathbf{n} = (\cos \theta, \sin \theta, 0)$, which at equilibrium is harmonic in the one-constant approximation, $\nabla^2 \theta = 0$ (see Sec. II A). Numerous methods of finding solutions immediately come forward, each impeded only by potentially complex boundary geometries, generically nonlinear boundary conditions, and topological constraints. An elegant approach to solving these problems uses complex variables and techniques, resulting in representations for generic particle shapes that are exact for the limit of strong anchoring boundary conditions, and asymptotically valid for large, finite anchoring strengths [84, 148, 149]. Figure 5(a) shows the equilibrium director lines for a two-dimensional LC field, which is uniform at infinity, with finite-strength tangential anchoring conditions on the surface of a triangular inclusion, computed with these techniques. For large but finite anchoring strengths, Dirichlet conditions can be assumed on a virtual surface just inside the boundary, which leaves both the fluid equations and the boundary conditions invariant under a conformal mapping.

For multiple bodies, conformal mapping techniques for multiply connected domains established by Crowdy and collaborators [150] unlock exact and approximate interaction potentials between particles in LCs. This complex variable approach allows for the analytical computation of particle

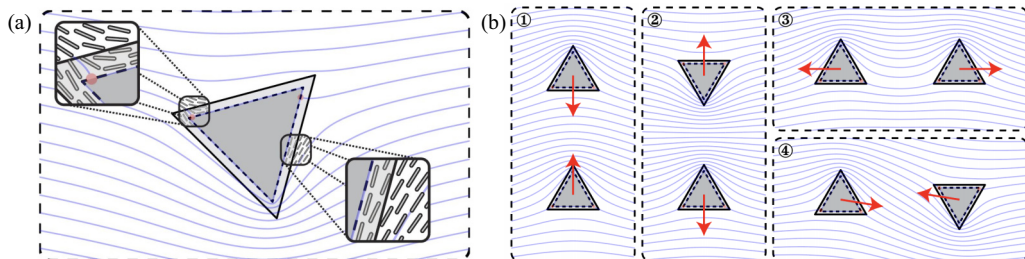


FIG. 5. (a) Director lines around an immersed triangular body in two dimensions; Dirichlet boundary conditions may be assigned on a virtual surface (dashed lines) just interior to the actual body surface, a critical step when using conformal mapping techniques with a finite anchoring strength. Reproduced from Ref. [84]. (b) Two triangular particles attract or repel depending on their relative orientations, and positioning relative to the background director field (horizontal in all cases shown). There is no net torque acting on each triangle, and the arrows indicate the direction of force. Reproduced from Ref. [147].

interactions at arbitrary positions and orientations, not just in the far field. Figure 5(c) shows the director fields so produced, along with net forces indicated by red arrows, for two triangular particles positioned and oriented in different configurations relative to the (horizontal) background director field. Each triangle is in a local rotational equilibrium, with no net torque acting on it. Particle repulsion and attraction, as in the experiment shown in Fig. 4(e), were reproduced analytically [147].

IV. DEFORMABLE BODIES

The elastic energy stored in an LC with immersed rigid particles can be reduced by particle translation and rotation, giving rise to the nontrivial interactions of colloids discussed above. An additional means of energetic relaxation arises when those particles, or any confining boundaries, are deformable. In this case, a competition emerges between the effects of the bulk elasticity and body elasticity, which selects energy minimizing boundary shapes. Recent efforts have included LC-mediated deformations of vesicles and more complex cells, as we will discuss. But we begin this section by reviewing a related system, finite LC domains immersed in an isotropic phase, known as tactoids.

A. Tactoids

Although droplets are not often considered bodies, finite LC domains immersed in an isotropic phase (“tactoids”) reveal some of the most important features of fluid-structure interactions in LCs. In particular, tactoids are not spherical. Instead, they tend to deform so as to reduce the degree of LC deformation, while satisfying the anchoring conditions, as shown in Fig. 6(a). The tactoids are viewed through cross-polarizing lenses, and the shading corresponds to a dipolar LC configuration inside each droplet [151]. As a thought experiment, a tactoid of fixed volume, elongated to a needle shape, places no elastic burden on the LC, as modeled for instance by Eq. (1). Resisting this elongation, however, is a surface tension between the isotropic and nematic phases, and ultimately shapes of finite aspect ratio are observed. This elongation may also be understood by considering the surface tractions on a rigid body with tangential anchoring conditions, as shown in Fig. 3(a).

Since tactoid shape selection is due to the competition between the bulk elastic energy and the surface tension, the degree of tactoid elongation depends on its size, described for various limits by Prinsen and van der Schoot [38]. Their tidy energy scaling argument for elongated dipolar tactoids is as follows. Consider a prolate ellipsoidal tactoid with semimajor and semiminor axis lengths R and r , respectively, and volume $V = (4\pi/3)r^2R$. The free energy density is estimated by

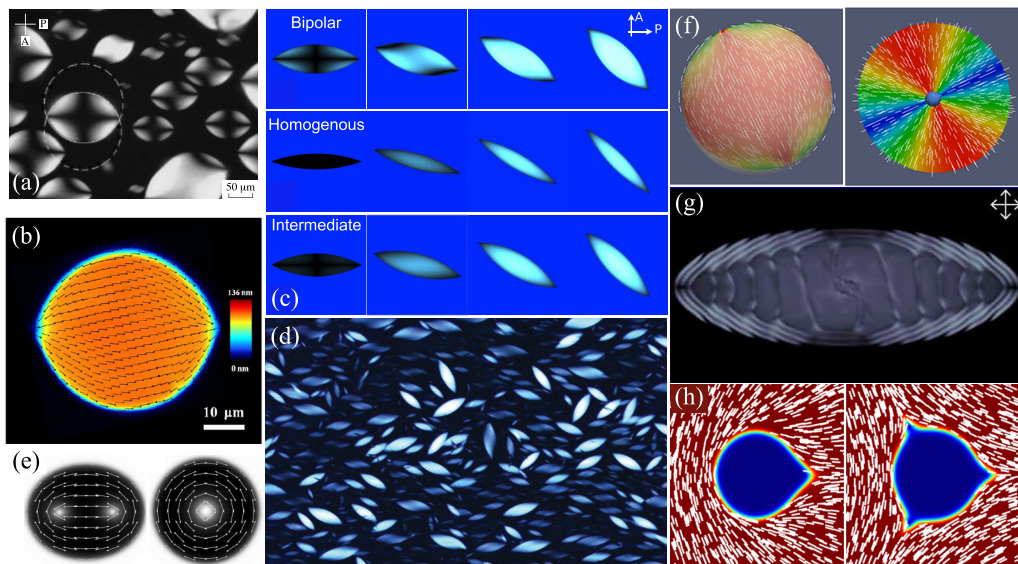


FIG. 6. Droplets of LC phases in isotropic environments, or tactoids, are elongated due to a competition between bulk LC elasticity and surface tension. (a) Dipolar LC configurations inside the tactoid are visible under cross-polarizers. Reproduced from Ref. [151]. (b) Larger droplets remain closer to spherical, and smaller droplets are more elongated, as reproduced in numerical simulations. Reproduced from Ref. [154]. [(c) and (d)] A population of tactoids shows a continuum of configurations, from bipolar to homogeneous (constant) director configurations. Reproduced from Ref. [155]. (e) A topological transformation in the interior of a tactoid, as two defects merge into one, by increasing the splay elastic constant, K_1 . Reproduced from Ref. [156]. (f) Reversible dipolar to radial transformations of the LC configuration can be triggered with the addition of surfactants. Reproduced from Ref. [157]. (g) More exotic LC droplet configurations are possible using chiral (cholesteric) LCs. Reproduced from Ref. [158]. (h) Negative tactoids (isotropic droplets inside nematic LCs) show localized deformations near topological defects. The background director field is that of a $+1/2$ defect (left) or a $-1/2$ defect (right). Reproduced from Ref. [159].

assuming strong tangential surface anchoring. Noting that $\nabla \cdot \mathbf{n}$ is on the order of $1/R$ and splay deformation is far larger than bending and twisting for elongated configurations, the Oseen-Frank energy density in Eq. (1) is approximated as $\mathcal{F} \approx (K_1/2)(\nabla \cdot \mathbf{n})^2 \sim K_1/R^2$. With the volume of the droplet V above, this suggests that the total bulk LC elastic energy scales like $\mathcal{E} \sim K_1 R(r/R)^2$. Meanwhile, the contribution of the surface tension energy scales roughly as γRr , with γ the surface tension. Balancing these two energies predicts the aspect ratio for a given volume,

$$\frac{R}{r} \sim \left(\frac{K_1}{\gamma} \right)^{3/5} V^{-1/5}. \quad (29)$$

Hence, smaller droplets are deformed more substantially, which will be seen again later with soft elastic shells. This may appear counterintuitive since droplets of isotropic media (inside other isotropic media) tend to be nearly spherical due to the growing importance of surface tension as the droplet size is reduced. More generally, tactoid elongation and shapes depend on the relative sizes of the Frank elastic constants [152]. Volume reduction, possible for some polymeric droplets, also leads to elongation and for small twist constants may also trigger a twist relaxation of the Williams type [86, 153].

An example of a large simulated LC droplet, which is only moderately stretched at equilibrium, is shown in Fig. 6(b) [154]. Smaller, and hence more elongated, tactoids are shown from experiments in Figs. 6(c) and 6(d). This population of tactoids actually shows a continuum of possible LC

configurations across a narrow region of droplet lengths, from bipolar configurations with “boojum” defects at the poles, to homogeneous (uniform) configurations [155].

Tactoid geometries can be studied more directly by considering local force balance. The surface energy density, \mathcal{F}_s , defined in Sec. II A introduces an effective surface tension, which may or may not depend on surface anchoring conditions. For instance, replacing \mathcal{F}_s in Eq. (4) by a constant surface energy, $\mathcal{F}_s = \gamma$, a familiar surface tension arises in Eq. (20),

$$\nabla_s \cdot \mathbf{T}_s = \nabla_s \cdot [\gamma \mathbf{P}(\mathbf{v})] = 2\gamma\kappa\mathbf{v}, \quad (30)$$

with mean surface curvature $\kappa = -\nabla_s \cdot \mathbf{v}/2$, where $\nabla_s = \mathbf{P}(\mathbf{v}) \cdot \nabla$ is the surface del operator. If γ varies along the surface, then an additional tangential contribution, the Marangoni stress, appears as well. Volume-preserving deformations require global information; this constraint informs the selection of the pressure.

Beyond the aspect ratios and shapes of tactoids, their internal LC configurations offer additional intrigue. By varying the Frank elastic constants, the associated deformations are penalized differently, which can have striking consequences. Figure 6(e) shows a topological transformation inside a tactoid, caused by increasing the splay elastic constant, K_1 [156]. As splay becomes more costly, the bipolar configuration with two $+1/2$ defects (white dots) is abandoned in favor of a state with pure bend around a single central $+1$ defect.

Rearrangement of LC configurations can be more directly manipulated as well, which has put them in the spotlight for potential use in the design of functional materials [160,161]. For example, surfactants like sodium dodecyl sulfate (SDS) can be used to tune the internal LC configuration by changing the orientation of the LC molecules at the interface [157,162–164]. Figure 6(f) shows simulated droplets in a dipolar configuration (left), which can be changed to a radial configuration (right) on the addition of SDS. Bipolar to toroidal transitions are also possible [165]. Even more exotic chiral droplet shapes have been observed using cholesteric liquid crystals, an example of which is shown in Fig. 6(g) [158,164,166,167].

The inverted case, isotropic droplets immersed in a nematic phase (i.e., “negative tactoids”), show the formation of cusps as the droplet is locally pulled into the direction of topological defects, as shown in Fig. 6(h) [159]. Such local morphology changes can act to reduce the large elastic energy, associated with such defects, stored in the bulk LC [154]. These local deformations have also been observed in the gravitational rise of a Newtonian bubble in a nematic LC [168] and in entirely different settings, including GUVs in electric fields [169]. This general principle, predictable by considering the surface tractions on similarly shaped rigid particles (see Sec. II B) will be seen again shortly in other contexts.

Other areas of investigation on tactoid shape and structure include the role of confinement [88], finite constituent size [170], defect positioning [155], as well as their relevance in other areas of materials science [171–173], biological probing, and sensing applications [174–176] and in active biological machinery like the mitotic spindle [21,22,177–181]. The reader is also directed to Ref. [46], which includes a full chapter on mathematical modeling of droplets in LCs, including jump conditions that appear when handling surface cusps, special solutions, and the shapes of floating drops. Rigorous mathematical analysis in this area remains a topic of modern research [182].

B. Mathematical modeling—Surface elasticity

When a deformable body is immersed in a liquid crystal, its deformation modes depend on its material properties. To model the surface deformations caused by the LC tractions discussed in Sec. II B, a kinematic description of the deformation is needed. Looking ahead to the following sections, we first recall some of the standard modeling techniques used to study elastic deformations of an isotropic membrane; for further details see Refs. [183,184].

With X representing a point on an undisturbed reference surface, we denote by $\mathbf{x}(X)$ its current position (after deformation). Elastic energy depends on the surface displacement gradient, defined

by

$$\mathbf{F} = \mathbf{P}(\mathbf{v}) \cdot \frac{\partial \mathbf{x}}{\partial \mathbf{X}} \cdot \mathbf{P}(\mathbf{N}), \quad (31)$$

where \mathbf{N} and \mathbf{v} are the outward-pointing normals in the reference and current configurations, respectively, and $\mathbf{P}(\mathbf{v}) = \mathbf{I} - \mathbf{v}\mathbf{v}$ is a projection operator, as in Sec. II A. The surface (left) Cauchy-Green strain tensor, $\mathbf{F} \cdot \mathbf{F}^T$, then has eigenvalues λ_1^2 , λ_2^2 , and 0, with corresponding eigenvectors \mathbf{d}_1 , \mathbf{d}_2 , and \mathbf{v} [184,185]. Here λ_1 and λ_2 are the principle extension ratios measured along the deformation directions \mathbf{d}_1 and \mathbf{d}_2 in the tangent plane of the deformed surface. Following Skalak *et al.* [186], we define the surface strain invariants as $I_1 := \lambda_1^2 + \lambda_2^2 - 2$ and $I_2 := \lambda_1^2 \lambda_2^2 - 1$.

Stretching the membrane (i.e., $\lambda_i \neq 1$) results in internal membrane stresses, which can be written in terms of an in-plane Cauchy stress tensor \mathbf{T} . At equilibrium, these stresses must balance any external tractions acting on the surface, \mathbf{f} , according to $\mathbf{f} = \nabla_s \cdot \mathbf{T}$, where $\nabla_s = \mathbf{P}(\mathbf{v}) \cdot \nabla$ is the surface del operator—if this traction is due to an ambient LC, then \mathbf{f} is given by (20b). For example, for small strains ($|\lambda_i^2 - 1| \ll 1$), the internal membrane stresses are given by two-dimensional linear elasticity (i.e., Hooke's law), with stress tensor

$$\mathbf{T} = \frac{2G_s}{1 - \nu_s} [(1 - \nu_s)\mathbf{E} + \nu_s \text{Tr}(\mathbf{E}) \mathbf{P}(\mathbf{N})], \quad (32)$$

for the surface Green-Lagrange strain tensor $\mathbf{E} = (1/2)[\mathbf{F}^T \cdot \mathbf{F} - \mathbf{P}(\mathbf{N})] \approx \mathbf{P}(\mathbf{N}) \cdot (\mathbf{D} + \mathbf{D}^T) \cdot \mathbf{P}(\mathbf{N})$ and $\mathbf{D} = \partial \mathbf{x} / \partial \mathbf{X} - \mathbf{I}$. Here G_s and ν_s are the two-dimensional shear modulus and Poisson's ratio, respectively.

For larger strains, the Hookean approximation does not capture the nonlinear response of the material. A wide range of nonlinear elastic phenomena may instead be captured using a hyperelastic or Green material model. In an isotropic hyperelastic material, the relationship between strain and stress is governed by a material-dependent strain energy density, $\mathcal{W}(I_1, I_2)$, written in terms of the strain invariants above. The in-plane Cauchy stress tensor is then given by

$$\mathbf{T} = \frac{1}{J} \mathbf{F} \cdot \frac{\partial \mathcal{W}}{\partial \mathbf{F}} = \frac{2}{J} \left[\frac{\partial \mathcal{W}}{\partial I_1} \mathbf{F} \cdot \mathbf{F}^T + J^2 \frac{\partial \mathcal{W}}{\partial I_2} \mathbf{P}(\mathbf{v}) \right], \quad (33)$$

where $J^2 = I_2 + 1 = \det(\mathbf{F} \cdot \mathbf{F}^T + \mathbf{N}\mathbf{N})$, see Ref. [185]. If the surface is incompressible (area preserving), then a pressure term $-p\mathbf{P}(\mathbf{v})$ is added to \mathbf{T} above, where p acts as a Lagrange multiplier to enforce $J = 1$.

As a common example, the strain energy density for a two-dimensional neo-Hookean surface can be written as

$$\mathcal{W} = \frac{G_s}{2} \left(I_1 + \frac{1}{I_2 + 1} - 1 \right), \quad (34)$$

and then the Cauchy stress, from Eq. (33), is given by

$$\mathbf{T} = \frac{G_s}{J} \left[\mathbf{F} \cdot \mathbf{F}^T - \frac{1}{J^2} \mathbf{P}(\mathbf{v}) \right]. \quad (35)$$

This strain energy is derived from the isotropic volume-incompressible neo-Hookean model for three-dimensional rubberlike materials and assumes the membrane has a very small uniform thickness [183,187]. Here the area dilatation is unrestricted, but it is compensated by a thinning of the membrane (i.e., the material volume is preserved). In practice, this model is effective at modeling a wide-range of materials (at least for small strains). However, in general, it does not exhibit the material response seen at larger strains; for example, the weak resistance to shear and strong resistance to area dilatation seen in red blood cells [188].

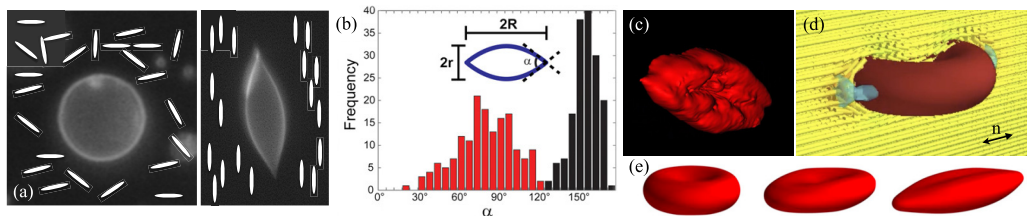


FIG. 7. Deformable bodies in nematic LCs stretch to relieve the fluid’s stored elastic energy. (a) A giant unilamellar vesicle (GUV) is spherical when the surrounding (and internal) LC is in the isotropic phase. The LC quenches into the nematic phase below a critical temperature, and the GUV stretches along the director axis. The spherical vesicle has diameter $10\ \mu\text{m}$, and the directors are schematic. Reproduced from Ref. [39]. (b) When deformed by the LC, larger GUVs remained nearly spherical, while smaller GUVs were highly elongated, but with a substantial volume decrease suggesting a possible rupture and fluid efflux. Reproduced from Ref. [39]. (c) A 3D reconstruction of Z-stack images obtained through confocal microscopy of a red blood cell, stretched by the interaction with a surrounding nematic LC. Reproduced from Ref. [42]. (d) A stiff biconcave disk (discocyte) with tangential anchoring conditions rotates until its line of symmetry is orthogonal to the background director field in simulations; two defects appear at the fore and aft points on the surface (isocontours of scalar parameter $S = 0.4$ are shown in blue). Reproduced from Ref. [42]. (e) A softer cell is stretched in direction of the background field, and perpendicular to its initial line of symmetry, extending the simulation in (d). Reproduced from Ref. [42].

In the Skalak model of red blood cells [186,189], the deformation away from an initial biconcave configuration is penalized by the strain energy density,

$$\mathcal{W} = \frac{E_S}{4}(I_1^2 + 2I_1 - 2I_2) + \frac{E_D}{8}I_2^2, \quad (36)$$

where E_S and E_D are the (constant) elastic shear and area dilation moduli, respectively, which have units of energy per area (see also Refs. [187,188,190–192]). Common values are $E_S = 4.2 \times 10^{-6}\ \text{N/m}$ and $E_D = 10^{-4}\ \text{N/m}$ [189,190,193]. From Eq. (33), we have

$$\mathbf{T} = \frac{E_S}{2J}(I_1 + 1)\mathbf{F} \cdot \mathbf{F}^T + \frac{J}{2}(E_D I_2 - E_S)\mathbf{P}(\mathbf{v}). \quad (37)$$

For a review of other hyperelastic energies used to model lipid bilayers, and for use in other biological settings, see Refs. [194,195].

C. Vesicles, membranes, cells, and shells

While droplets often separate two fluids or fluid phases by little more than surface tension, other barriers involve additional components, as is the case with molecular monolayers and membranes. These thin layers introduce additional energetic costs to deformation, which now enter the balancing act with the bulk and surface LC energies when determining equilibrium particle shapes.

As an example, Fig. 7(a) (left) shows a giant unilamellar vesicle (GUV) in the isotropic phase of DSCG, a lyotropic chromonic LC, which is believed to confer finite-strength tangential anchoring conditions on the LC that is both exterior and interior to the surface. When the temperature is cooled below a critical value, an isotropic-to-nematic phase transition occurs and elongated GUVs are instead observed, like that in Fig. 7(a) (right). In this study by Mushenheim *et al.* [39], two distinct populations were observed: Like tactoids, smaller GUVs were elongated and spindlelike, while large GUVs were more spherelike. The smaller GUVs showed a substantial reduction in volume through the isotropic-to-nematic transition, seen via the bimodal opening angle statistics in Fig. 7(b). However, while large surface area changes of tactoids are inhibited by surface tension, GUVs are nearly inextensible, presenting a much stiffer constraint. A sphere cannot deform at fixed volume without changing its surface area; thus, only vesicles with a reduced interior volume can be

substantially elongated. This indicates that the GUVs likely ruptured in the process of quenching from the isotropic to the nematic phase, and internal fluid escaped to the surrounding environment, thus allowing for more substantial elongation. More complex geometries can also emerge in this relaxation process. Jani, Nayani, and Abbott used this observation of efflux to generate a wide variety of GUV shapes, which appeared on phase cycling from the isotropic to nematic phase and back again [41].

Vesicles are composed of lipids which are free to move throughout the surface, and there is no elastic penalty to in-plane shearing. Vesicle bending, however, does elicit an elastic response, characterized by its bending rigidity. A common model is the Canham-Helfrich energy,

$$\mathcal{E}_b = \int_{\partial\Omega} \gamma + \frac{k_c}{2} (2H - c_0)^2 + \bar{k}K \, dA, \quad (38)$$

where γ is a surface tension, H and c_0 are the mean and spontaneous or preferred curvature, K is the Gaussian curvature, and k_c and \bar{k} are the bending and saddle-splay moduli [196–198]. For closed, smooth surfaces the integrated Gaussian curvature is invariant (the Gauss-Bonnet theorem links this quantity to the surface topology alone) and the third term may be neglected. For more complete discussions see Refs. [199,200].

The shapes of more complex cells have also been explored in a nematic LC. Red blood cells at rest, for instance, take the shape of a discocyte (a biconcave disk). Their material and geometric properties include a significant shear elasticity owing to the spectrin network internal to the membrane, a large dilational modulus, and a relatively small reduced volume (a smaller volume than that of a sphere with the same surface area). Figure 7(c) shows a three-dimensional (3D) reconstruction of Z-stack images obtained by Nayani *et al.* [42] through confocal microscopy of a red blood cell, stretched by interaction with a surrounding nematic LC. Simulations were then used to infer material properties of the cell from this deformation. Figure 7(d) shows a rigid biconcave disk (discocyte) inside a nematic LC, modeled using the \mathbf{Q} -tensor theory described in Sec. II A, with finite tangential anchoring boundary conditions assumed. The cell first rotates so that its line of symmetry is perpendicular to the direction of the background director field, and two defects appear at the fore and aft points on the cell; an isocontour of the scalar order parameter, $S = 0.4$, is shown in blue.

Figure 7(e) shows the quasistatic relaxation of this Skalak model red blood cell [see Sec. IV B, particularly Eq. (36)] inside the nematic LC. The cell elongates in the direction of the background director field and orthogonally to its initial line of symmetry. Two lobes remain in the ultimate state, revealing memory of the cell's resting geometry. Due to the large dilational modulus for red blood cells, the deformation is nearly inextensible, and bending energy (which is not included in the Skalak model) is negligible. Instead, the surface deformation is dominated by shear strain [42]. Additional cell types, including human Schwann cells, have also very recently been probed using this methodology [201].

Homeotropic (normal) anchoring conditions can result in a different mode of deformation. Figure 8(a) shows the quasistatic relaxation of a simulated vesicle with strong homeotropic anchoring conditions [40]. In this case, the presence of the undeformed (spherical) particle results in a Saturn-ring defect, shown as a melted region (a region with a diminished scalar order parameter, S) in blue. If the particle is allowed to deform, however, then the sphere bulges outward towards the Saturn-ring, providing that high-energy region with a surface on which to better match the anchoring conditions. This is at the cost, however, of an increased surface bending and stretching energies. This is consistent with the deformation suggested by viewing the traction field on a rigid particle (even in two dimensions) with the appropriate bulk topological defects [see Fig. 3(d)].

When the Frank energy of the bulk LC is small compared to membrane bending stiffness, surface tension, and surface anchoring energy, as is the case for small membranes, a Laplace-Helfrich equation describing the membrane shape may be derived [202]. Just as for membranes containing and immersed in isotropic fluids [203], intricate phase diagrams of membrane shapes emerge. Figure 8(b) shows a ternary phase diagram across a range of membrane bending stiffness, k_c ,

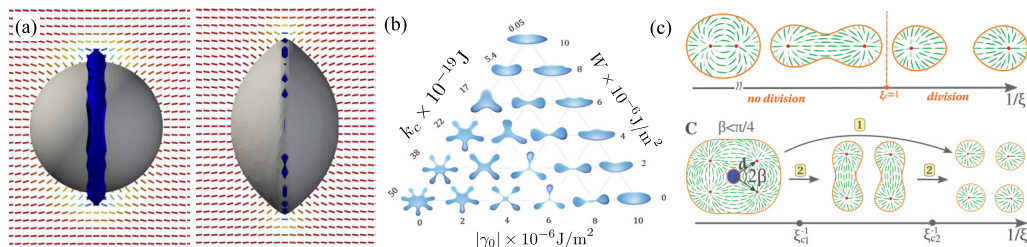


FIG. 8. (a) A simulated vesicle with homeotropic (normal) anchoring deforms in the direction of its Saturning defect, increasing the elastic energy stored in the vesicle, but decreasing the elastic energy stored in the nematic LC. Reproduced from Ref. [40]. (b) A ternary phase diagram for two-dimensional LC membranes over a range of membrane bending stiffness, k_c , surface tension, γ_0 , and anchoring strength, W . Reproduced from Ref. [202]. (c) Constant area shapes of two-dimensional nematic droplets with elastic boundaries with two +1 defects. Top: division is energetically preferred above a critical shape parameter; bottom: division can occur directly into four cells, or indirectly through two intermediate droplets. Reproduced from Ref. [204].

surface tension, γ_0 , and anchoring strength, W . When bending elasticity and anchoring strength are of comparable size, up-down symmetry breaking is observed; and, as the surface tension is reduced, the wave number of surface deformations increases. When the anchoring strength is small, classical membrane shapes are found. But at large anchoring strength, spindle shapes appear yet again, even though the bulk LC energy has been neglected.

The analog of negative tactoids in this setting are deformable membranes or shells which contain an LC in their interior. Of particular recent interest are the shapes of cell membranes which emerge in conjunction with active internal nematic stresses (see Sec. V). As a stepping stone, Leoni *et al.* studied the geometries and division of nematic LCs in two dimensions with elastic boundaries, and internal +1 defects modeling centrosomes in the mitotic spindle [204]. Figure 8(c) (top) shows a progression of energy-minimizing solutions depending on a single shape parameter, which incorporates active processes and controls centrosome separation; division occurs above a critical value. Four model centrosomes can directly divide the original cell into four daughter cells, or indirectly, through two intermediate droplets, Fig. 8(b) (bottom).

The line is blurred between LC droplets and elastic shells when surfactants are introduced to the system. Surfactants can bind to a droplet or tactoid interface, conferring additional surface physics, from rigidification to surface gradients leading to Marangoni stresses. Early probes into the shapes of droplets that incorporate elastic surface moduli include work by Lishchuk and Care [162] and Silvestre *et al.* [47], and then by Mackay and Denniston, who computed the equilibrium shapes of one elastic shell and two interacting shells in an anisotropic fluid [205], to be discussed in Sec. IV E.

D. Nematic surfaces

Some soft materials themselves have internal nematic order. The surface shape is then governed by in-plane elastic LC stresses, along with with additional costs associated with surface tension (nematic films) and/or costs due to out-of-plane deformations, which are different for vesicles or membranes and shells.

We have already seen how the tractions on rigid colloids are suggestive of the deformations that will ensue when a body is made compliant. Similarly, the equilibrium in-plane nematic order on rigid surfaces offers insight into the deformation modes of soft nematic surfaces. In particular, topological defects are points of elevated, or potentially extreme, elastic stress, which will be given a new opportunity to relax when the surface is made deformable. Accordingly, the resulting force balance can result in a variety of equilibrium shapes. On a rigid sphere, in the one-constant

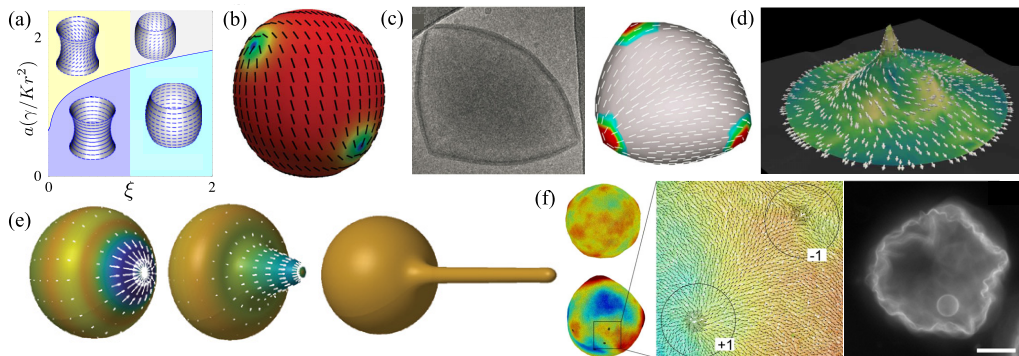


FIG. 9. (a) Equilibria of a film with in-plane nematic ordering, with strong tangential anchoring on the boundaries. Bifurcations from homogeneous to inhomogeneous ordering (akin to a Fréedericksz transition) arise beyond a critical value that depends on the relative surface tension to Frank elastic constant, for a given boundary distance-to-radius ratio, $\xi = h/r$. Modified from Ref. [216]. (b) Deformation of a sphere using a Landau–de Gennes–Helfrich model, with two of the four $+1/2$ defects visible. Color represents the scalar order parameter, S , which diminishes near the defects. Reproduced from Ref. [227]. (c) A smectic polymer vesicle (left) and simulated nematic vesicle (right) deform in the directions of topological defects into tetrahedral shapes. Reproduced from Ref. [219]. (d) Spiral in-plane ordering of an active nematic, buckled into a funnel-like profile with a topological defect at the tip. Reproduced from Ref. [230]. (e) Surface morphogenesis of active epithelial cells with nematic ordering show pronounced tubulation, in stark contrast to a growing isotropic shell. Reproduced from Ref. [231]. (f) Left: simulations of a fluctuating nematic surface reveal kinetic trapping of defects, which are circled in the central panel. Right: fluorescence microscopy of a lipid vesicle (DPPC) with in-plane ordering and molecular tilt, crumpling below a critical temperature for isotropic-to-nematic phase transition. (Scale bar 20 μm). Reproduced from Ref. [220].

approximation, four $+1/2$ defects relax to the vertices of a tetrahedron [206], while if bending is much more costly than splaying, then they may instead collapse onto a great circle [207] (see also Refs. [208–212]). For a closed vesicle or membrane that takes the form of a topological sphere, i.e., a genus-0 surface, the Gauss-Bonnet theorem states that the total topological charge of a nematic confined to the local tangent plane is an invariant; specifically, the charges must add up to 2. On a torus, defects need not be present, though the dynamic process of relaxation and annihilation of defects can depend on the surface curvature [213].

The energy of a nematic film pairs Frank elasticity with surface tension [214–216]. An example of such a free energy with the one-constant approximation is

$$\mathcal{E} = \int_{\partial\Omega} \gamma + \frac{K}{2} \|\nabla_s \mathbf{n}\|^2 dA, \quad (39)$$

where \mathbf{n} is confined to the local tangent plane on the surface, γ is a surface tension, and $\nabla_s = \mathbf{P}(\mathbf{v}) \cdot \nabla$, as in Sec. IV B. Figure 9(a) shows the equilibrium configurations of a film with in-plane nematic ordering and strong tangential anchoring on two circular boundaries of radius r , separated by a distance h [216]. The relative separation distance, $\xi = h/r$, affects the inward or outward bulging of the film, and for a sufficiently large value of the dimensionless group, γ/Kr^2 , there is a bifurcation from homogeneous to inhomogeneous ordering (akin to a Fréedericksz transition, [2]). For a discussion on thin film modeling and the stability of nematic films, see Ref. [217].

Nematic vesicles and some membranes are composed of components that may move freely as a fluid layer (or often a bilayer), or become polymerized [218–220]. Such systems pair Frank elasticity with a Helfrich surface energy like that in Eq. (38). Vesicles and membranes with in-plane nematic ordering can relax into prolate and cylindrical geometries [211,221], toroidal shapes [206], and pseudospheres (shapes of constant negative Gaussian curvature) [222] and may result in tubulation

[223]. Although tubulation and elongation are commonly observed, in-plane order can also suppress the formation of membrane necks, depending on the molecular tilt order on the surface [224].

Due to the requirement of defects on closed surfaces, as previously noted, the in-plane LC elasticity is often described using an energy based on a surface tangential \mathbf{Q} tensor. A Landau–de Gennes–Helfrich model energy couples this with membrane bending costs (see Refs. [212,225–227]). Figure 9(b) shows the deformation of a sphere using such a model, with the surface colored by the scalar order parameter S . The scalar order decreases near the four $+1/2$ defects, two of which are visible in the image [227]. It is notable that the energy minimizing configuration does not combine defects into two $+1$ defects, placed at the poles of an axisymmetric tactoidlike shape, which might be expected. On reducing the internal volume, the tetrahedral arrangement of defects can result in a more pronounced surface deformation. Figure 9(c) shows a smectic polymer vesicle and accompanying simulation [219]. The resulting shapes can vary considerably depending on the relative bending-to-splaying energetic costs. Passive selection of shapes in this way may allow for the design of new classes of responsive supramolecular structures and materials [228,229].

Nematic shells, meanwhile, can relax into somewhat more complex shapes, including stomatocytes and elongated, bulbous shapes [232], and other exotic geometries, for example those shown in Fig. 8(b). Such inquiries extend classical work on membrane shapes with isotropic elastic energy densities [203,233,234]. Mathematical analysis addressing questions of existence of minimizers and well-posedness in nematic shells have been taken up in Refs. [235–237].

More complex out-of-plane energies require more substantial modeling, as is used to describe LC elastomers [238,239]. Modes of LC elastomer deformation not generally seen in films and vesicles, like wrinkling, are commonly observed [240–242]. LC elastomers have also been used as a programmable material, capable of generating complex desired topographies [243–245].

Finally, colloidal membranes—liquidlike monolayers composed of aligned, rod-shaped particles—share similarities with nematic surfaces. These membranes, which are typically one rod-length thick, may not lie perfectly in the tangent plane, but their morphology is again dictated by a balance of in-plane fluidlike dynamics and out-of-plane bending elasticity [246,247]. Particularly if the constituents are chiral, a great variety of membrane shapes can emerge, from catenoids to Enneper surfaces [248–250].

Although outside of the scope of this review, when nematic order is accompanied by active stresses, associated membrane shapes are not only exotic, but dynamic and chaotic [251–254]. For a detailed symmetry-based theory covering nematic and polar active surfaces see Ref. [255]. Figure 9(d) shows an active nematic, with spiral in-plane ordering, buckling into a funnel-like profile with a topological defect at the tip [230], while Fig. 9(e) shows the tubulation during the growth of model epithelial cells confined to a topological sphere [231]. These deformations lie in stark contrast to the dynamics expected with isotropic in-plane mechanical stresses [230]. In-plane order can also strongly affect the nature of membrane fluctuations. Figure 9(f) shows an image from experiments using a lipid vesicle with in-plane ordering and molecular tilt, with accompanying simulations, crumpling below a critical temperature for isotropic-to-nematic phase transition [220]. In this study, kinetic trapping of defects in strongly curved regions, circled in the central panel of Fig. 9(f), prevented their relaxation or annihilation.

Templating out-of-plane deformations by defects is used frequently in biological systems, though generally in more active settings like those noted above. Defect-induced stresses are a precursor to epithelial cell death and extrusion [256] and morphogenesis [230,231,257], can suppress cancer cell clearance from a mesothelial monolayer [258], and can affect the dynamics of neural stem cells in the central nervous system [259].

E. Multiple deformable bodies

The combination of elastic particle deformability and interaction has thus far seen relatively little attention, perhaps owing to the substantial difficulties involved in modeling, solving, and characterizing such complex systems. A notable early work is by Mackay and Denniston, who

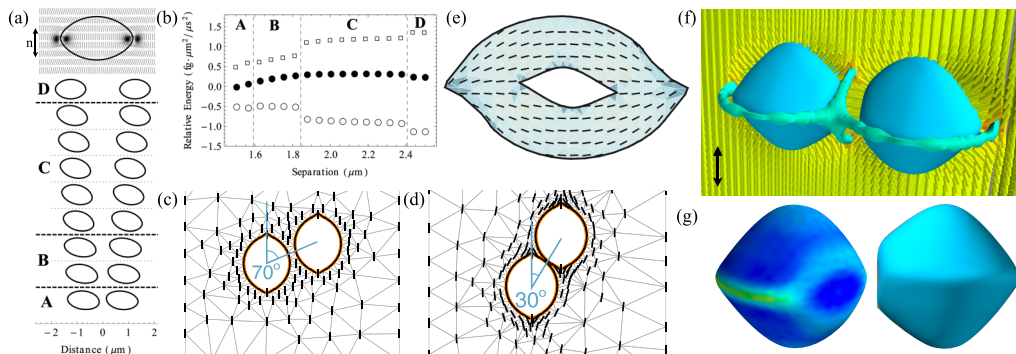


FIG. 10. (a) Two deformable bodies with homeotropic (normal) anchoring approach each other over time, stretching as they draw near, and deforming antisymmetrically as their defects locally repel. Reproduced from Ref. [205]. (b) The surface elastic energy (hollow circles), LC elastic energy (hollow squares), and the total energy (their sum; black circles) associated with the progression in (a). The individual energies show multiple discontinuities in the separation distance. Reproduced from Ref. [205]. [(c) and (d)] Two shells in two dimensions initially repel then attract, and find an equilibrium alignment angle. Reproduced from Ref. [260]. (e) Chiral deformation instability of a deformable boundary due to a deformable internal inclusion. Reproduced from Ref. [261]. (f) Two deformable shells with homeotropic (normal) anchoring conditions connected by an entangled hyperbolic (figure of theta) defect (courtesy Art Evans). (g) The deformed shapes in (f); colored by bending energy (left), revealing both flat (developable) regions and a sharp ridge extending towards the Saturn-ring disclination.

showed the attraction of two deformable shells with homeotropic (normal) anchoring conditions in two dimensions [205]. Figure 10(a) shows a progression in time of two such circular shells. Most immediately noticeable is their individual elongation, as expected from Fig. 3(d), and like that in three dimensions in Fig. 8(a). Next, the bodies attract, followed by symmetry breaking deformations. This symmetry breaking is reminiscent of the surface defect rearrangement noted for two rigid particles [85,147], which tend to locally repel each other. Here, however, the motion of the defects is accompanied by surface deformations in those directions. More subtle are a sequence of discontinuities in the relative energy. Figure 10(b) shows the associated changes in the surface stretching energy (hollow circles), bulk LC elastic energy (hollow squares), and their sum (black circles) as a function of the separation distance. While the total energy appears continuous in the separation distance, there are multiple discontinuities in the individual energies. Two rigid cylinders show a single energy discontinuity in the separation distance due to a pitchfork bifurcation in the defect positions [147]; with deformable shells, in this case three such discontinuities are observed. The number of discontinuities depends on the surface material properties [205].

If instead tangential anchoring conditions are used, then a different configuration is observed. Figures 10(c) and 10(d) show the initial and final positions, respectively, of two elastic shells in two dimensions, with a vertical background director field. The shells initially repel then attract and settle to an equilibrium alignment angle of roughly 30° . This alignment angle was found to decrease as the body aspect ratio increased [260]. It is not uncommon to find symmetry breaking in multibody interactions even with rigid particles in nematic LCs, for instance in the examples shown in Figs. 4(b) and 4(h), and we observe this again here with deformable particles. Figure 10(e) shows an additional example of symmetry breaking with deformable boundaries. In this case a nematic LC is confined to a deformable annulus with tangential anchoring conditions. The outer and inner boundaries elongate to reduce the bound elastic energy in the LC, but a chiral symmetry breaking deformation is observed [261,262].

Symmetry-breaking positioning and deformations need not always emerge in LC-mediated particle interactions. Some highly deformed bodies can find a symmetric equilibrium state, even

with complex topological singularities in the fluid. Figure 10(f) shows simulations of two linearly elastic shells with homeotropic anchoring, their individual Saturn-ring defects having merged into a single entangled hyperbolic (figure of theta) defect, similar to those found using rigid particles, Figs. 4(c) and 4(d). This configuration was computed using a linearly elastic shell penalizing stretching and bending, and the \mathbf{Q} tensor theory via an immersed boundary approach (as in Ref. [42]). The shapes of these symmetrically deformed shells are shown in Fig. 10(g); the body on the left is colored by the bending energy in the shell, which shows a sharp ridge of bending along the edge extending outwards towards the Saturn-ring defect, as in Fig. 8(a), and an additional ridge extending towards the ring-shaped defect in between them. The regions of the bodies closest to each other are flat, which is preferred both by the homeotropic anchoring conditions (the LC direction can extend directly from one surface to the other without bending or splaying), and the bending energy in the elastic shell is also zero. The LC energy-relieving body deformations have promoted the appearance of developable surfaces, ruled surfaces with zero Gaussian curvature. General principles of elastic surface energy minimization begin to come into view [200,263].

V. CONCLUSIONS AND OUTLOOK

In this review, we have aimed to present some of the fundamental features of soft body deformations by liquid crystalline environments in the nematic phase, as well as the mathematical tools needed to study them. Even at equilibrium, such systems are not simply characterized, or analyzed, outside of special circumstances. But broadly speaking, soft bodies and inclusions deform in order to reduce the elastic burden on the bulk LC, but in such a way that their own surface energy is not greatly increased. Elongation of tactoids and elastic shells with tangential anchoring is one example. Local deformations near topological defects to better satisfy anchoring boundary conditions is another. Analysis of one and many rigid particles still provides a great deal of information, since the surface tractions from the bulk and surface LC energies informs which deformations will ensue if immersed bodies are made compliant.

Even within the class of problems involving elastic media immersed in a nematic LC, there are many additional directions of immediate interest. Forests of deformable fibers immersed in a nematic LC can bend when the director field is manipulated, e.g., with an electric field [264,265]. And, commonly, membranes themselves possess orientational order, which has seen substantial theoretical investigation. We only scratched the surface of this flourishing area in Sec. IV D.

Given the degree of nonlinearity and the wide separation of length scales inherent to the systems described, continued development of fast and accurate numerical methods is needed. Immersed boundary methods that have been used to study soft particles in Oldroyd-B viscoelastic fluids [266–270] have also been used to study them in nematic LCs [42,68,271–273]. However, the accuracy of these methods can suffer when used in settings where gradients in the bulk fluid are needed (e.g., the Ericksen stress), to the point of nonconvergence, even if some bulk measures like net forces (or quasistatic relaxation) do converge [274]. Griffith and Patankar review a broader class of immersed interface methods in Ref. [275]. Other approaches applicable for nematic LCs include the finite element method [276], diffuse interface methods [277,278], and the use of radial basis functions [66]. Related methods for viscoelastic flows that might be modified for use with nematic LCs include an immersed-finite-element method [279], immersed boundary-lattice Boltzmann method [40,280–282], and a front-tracking approach [283]. Numerical interfacial rheology on its own requires care; for an overview of related numerical methods see Ref. [284].

There are hydrodynamic analogs of the systems presented here that have received parallel attention [285]. For instance, bodies moving through LCs can experience anisotropic viscous drag, which can be strongly nonlinear in the velocity [73,286–289], unlike the linear drag characteristic of classical viscous flows [290]. The deformable bodies immersed in the LC may even be bacteria or other microorganisms, interacting with the environment through both elastic and anisotropic viscous stresses [12]. The bulk LC field can be used to steer swimmer trajectories [11–13], and different topological defects can induce different bacterial accumulation or depletion [291,292]. Undulatory

motions have been studied theoretically [293] and numerically [272,273]; fluid anisotropy reveals substantial effects on swimming speeds, and even swimming directions. Pair interactions between two active particles immersed in an LC can depend on surface anchoring conditions [294]. In some cases the LC leads to swimmer repulsion; in others, collisions and group swimming have been observed [295]. And, as briefly introduced in Sec. IV D, adding activity to a nematic LC shell can produce wildly chaotic vesicle deformations and in-plane flows.

Meanwhile, the shapes and dynamics of deformable media by active stresses is a research area that dovetails with work on active gels [296] and locomotion in complex fluids and complex environments [28,297–299]. The deformable body may even be motile, as is the case for some LC droplets. Marangoni stresses can couple to internal elastic modes, resulting in coherent swimming, and generic symmetry breaking can result in chiral trajectories [300,301]. Reviews of this rapidly growing branch of the literature can be found in Refs. [302,303].

Looking ahead, experiments continue to be performed at a blistering rate, examining the functional consequences of biological cell shapes, and what can be gained by their manipulation. Measuring the elastic properties of cells using LCs is predicted to move into broad territory, given its natural benefits over more delicate methods like stretching with optical tweezers [304]. When biofilaments like microtubules or actin confer bulk LC elasticity to a fluid, particularly when activated by molecular motors or other active stresses, it is even more natural to inquire about the functional roles of the resultant enclosing membrane shapes. Analysis of surface tractions and body shapes, which incorporate not only the fluid elastic stress but also active stresses and their associated flows, is yet another direction that will undoubtedly continue to flourish in the near future.

Reinitzer, Lehmann, and other early pioneers of liquid crystal physics would surely be astonished to see how many different areas it has now informed, even extending to the shapes and function of biological cells. We hope for and expect such amazement when looking back on the next decades of research on deformable media in liquid crystalline environments.

ACKNOWLEDGMENTS

Long-running collaborations and discussions with Nicholas Abbott, Thomas Powers, Michael Graham, Art Evans, Ski Krieger, Eric Lauga, Gwynn Elfring, Timothy Atherton, David Stein, Michael Shelley, and Jean-Luc Thiffeault are gratefully acknowledged. Support was provided by the NSF (DMR-2003807) and the Office of the Vice Chancellor for Research and Graduate Education with funding from the Wisconsin Alumni Research Foundation.

APPENDIX: VIRTUAL WORK PRINCIPLE

In this Appendix, we derive the equilibrium forces and torques associated with a nematic LC confined to a domain Ω and subject to anchoring conditions on the boundary $\partial\Omega$. We shall start by considering the simpler theory, based on a director field \mathbf{n} , in Sec. A 1. We then go on to consider the Landau–de Gennes \mathbf{Q} -tensor theory in Sec. A 2.

1. Director field theory

We first derive the equilibrium forces and torques associated with a nematic LC delineated by a director field $\mathbf{n}(\mathbf{x})$, with spatial position \mathbf{x} and $|\mathbf{n}| = 1$. Similar derivations and further details can be found in Refs. [2,46,93,102]. Here the net energy of the system is assumed to take the form

$$\mathcal{E} = \int_{\Omega} \mathcal{F}(\mathbf{n}, \nabla \mathbf{n}) - \frac{\lambda}{2} (|\mathbf{n}|^2 - 1) dV + \int_{\partial\Omega} \mathcal{F}_s(\mathbf{n}; \mathbf{v}, \boldsymbol{\tau}) - \frac{\mu}{2} (|\mathbf{n}|^2 - 1) dA, \quad (\text{A1})$$

for the bulk energy density \mathcal{F} , e.g., Eq. (1); surface energy density \mathcal{F}_s , e.g., Rapini-Papoular, Eq. (5), or degenerate planar anchoring, Eq. (6); and Lagrange multipliers λ and μ , which impose $|\mathbf{n}| = 1$.

a. Energy variation

There are two mechanisms by which the energy may be reduced: The molecules may translate or rotate in place. These correspond to a variation in the spatial position $\tilde{\mathbf{x}} = \mathbf{x} + \mathbf{u}(\mathbf{x})$, with displacement vector $\mathbf{u} := \delta\mathbf{x}$, and the director field $\tilde{\mathbf{n}}(\tilde{\mathbf{x}}) = \mathbf{n}(\mathbf{x}) + \mathbf{r}(\mathbf{x})$, with the Eulerian variation $\mathbf{r} := \Delta\mathbf{n} = \delta\mathbf{n} + \delta\mathbf{x} \cdot \nabla\mathbf{n}$. The Lagrangian variation of the director field, \mathbf{n} , has already been described in Sec. II A, leading to the equilibrium equations, Eq. (10) subject to Eq. (11). The variation in position adds an extra layer of complexity to the variational problem. Here we denote the deformation matrix as $\mathbf{F} = (\partial\tilde{\mathbf{x}}/\partial\mathbf{x})^T = \mathbf{I} + \nabla\mathbf{u}^T$ and shall only consider incompressible deformations, i.e., $\nabla \cdot \mathbf{u} = 0$.

Since incompressible, the infinitesimal volume element is conserved, i.e., $\tilde{dV} = \det \mathbf{F} dV \sim dV$. The infinitesimal area element, however, varies according to Nanson's formula,

$$\tilde{dA} = \det \mathbf{F} |\mathbf{F}^{-T} \cdot \mathbf{v}| dA \sim (1 + \mathbf{P}(\mathbf{v}) : \nabla_s \mathbf{u}) dA, \quad (\text{A2})$$

where \mathbf{v} is the unit normal vector pointing into the LC, $\mathbf{P}(\mathbf{v}) = \mathbf{I} - \mathbf{v}\mathbf{v}$ is the surface projection operator, and $\nabla_s = \mathbf{P}(\mathbf{v}) \cdot \nabla$ is the surface gradient. The surface normal and tangent vector vary according to

$$\tilde{\mathbf{v}} = \frac{\mathbf{F}^{-T} \cdot \mathbf{v}}{|\mathbf{F}^{-T} \cdot \mathbf{v}|} \sim \mathbf{v} - \nabla_s \mathbf{u} \cdot \mathbf{v} \quad \text{and} \quad \tilde{\boldsymbol{\tau}} = \frac{\mathbf{F} \cdot \boldsymbol{\tau}}{|\mathbf{F} \cdot \boldsymbol{\tau}|} \sim \boldsymbol{\tau} + \boldsymbol{\tau} \cdot \nabla_s \mathbf{u} \cdot \mathbf{P}(\boldsymbol{\tau}), \quad (\text{A3a,b})$$

respectively. Finally, we note that a variation of the gradient of the director field is

$$\tilde{\nabla}\tilde{\mathbf{n}} = \tilde{\nabla}\mathbf{n} + \tilde{\nabla}\mathbf{r} \sim \nabla\mathbf{n} + \nabla\mathbf{r} - \nabla\mathbf{u} \cdot \nabla\mathbf{n}. \quad (\text{A4})$$

Altogether, the above identities yield the functional derivatives of the energy densities,

$$\delta\mathcal{F} = \mathbf{r} \cdot \frac{\partial\mathcal{F}}{\partial\mathbf{n}} + (\nabla\mathbf{r} - \nabla\mathbf{u} \cdot \nabla\mathbf{n}) : \frac{\partial\mathcal{F}}{\partial\nabla\mathbf{n}}, \quad (\text{A5a})$$

$$\text{and} \quad \delta\mathcal{F}_s = \mathbf{r} \cdot \frac{\partial\mathcal{F}_s}{\partial\mathbf{n}} - (\nabla_s \mathbf{u} \cdot \mathbf{v}) \cdot \frac{\partial\mathcal{F}_s}{\partial\mathbf{v}} + (\boldsymbol{\tau} \cdot \nabla_s \mathbf{u} \cdot \mathbf{P}(\boldsymbol{\tau})) \cdot \frac{\partial\mathcal{F}_s}{\partial\boldsymbol{\tau}}, \quad (\text{A5b})$$

and, hence, the functional derivative of the net energy

$$\delta\mathcal{E} = \int_{\Omega} \delta\mathcal{F} - \lambda\mathbf{n} \cdot \mathbf{r} - p(\nabla \cdot \mathbf{u}) dV + \int_{\partial\Omega} \delta\mathcal{F}_s + \mathcal{F}_s(\mathbf{P}(\mathbf{v}) : \nabla_s \mathbf{u}) - \mu\mathbf{n} \cdot \mathbf{r} dA, \quad (\text{A6})$$

where p is a Lagrange multiplier imposing incompressibility ($\nabla \cdot \mathbf{u} = 0$). Inserting Eq. (A5) into Eq. (A6) and integrating by parts (noting that $-\mathbf{v}$ is the outward pointing unit normal of the domain Ω) yields

$$\begin{aligned} \delta\mathcal{E} = & - \int_{\Omega} (\mathbf{h} + \lambda\mathbf{n}) \cdot \mathbf{r} + (\nabla \cdot \mathbf{T}) \cdot \mathbf{u} dV - \int_{\partial\Omega} (\mathbf{h}_s + \mu\mathbf{n}) \cdot \mathbf{r} + (\mathbf{v} \cdot \mathbf{T} + \nabla_s \cdot \mathbf{T}_s) \cdot \mathbf{u} dA \\ & + \int_{\partial\Omega} \nabla_s \cdot (\mathbf{T}_s \cdot \mathbf{u}) dA, \end{aligned} \quad (\text{A7})$$

for the bulk tensor, \mathbf{T} , and surface tensor, \mathbf{T}_s , defined in Eq. (21) and the bulk molecular field, \mathbf{h} , and surface molecular fields, \mathbf{h}_s , defined in Eq. (9).

b. Principle of virtual work

At equilibrium, the energy variation in Eq. (A7) is postulated to satisfy the principle of virtual work, as expressed in Eq. (19). To interpret this equation, we consider two specific cases. First, for an arbitrary infinitesimal displacement \mathbf{a} , for which $\mathbf{u} = \mathbf{a}$ and $\mathbf{r} = \mathbf{0}$, we obtain the conservation of linear momentum at equilibrium,

$$\delta\mathcal{E} = -\mathbf{a} \cdot \left(\int_{\Omega} \mathbf{F} dV + \int_{\partial\Omega} \mathbf{f} dA \right). \quad (\text{A8})$$

Thus, \mathbf{F} and \mathbf{f} are forces acting on the bulk (per unit volume) and the boundary (per unit area), respectively. The generalized forces, \mathbf{G} and \mathbf{g} , can be related to moments by considering an arbitrary infinitesimal rigid rotation $\boldsymbol{\omega}$, for which $\mathbf{u} = \boldsymbol{\omega} \times \mathbf{x}$ and $\mathbf{r} = \boldsymbol{\omega} \times \mathbf{n}$. Inserting these into Eq. (19) and rearranging yields

$$\delta\mathcal{E} = -\boldsymbol{\omega} \cdot \left(\int_{\Omega} \mathbf{x} \times \mathbf{F} + \mathbf{n} \times \mathbf{G} dV + \int_{\partial\Omega} \mathbf{x} \times \mathbf{f} + \mathbf{n} \times \mathbf{g} dA \right), \quad (\text{A9})$$

which, at equilibrium, describes the conservation of angular momentum. This yields the moment vectors acting on the bulk and the boundary, $\mathbf{M} = \mathbf{n} \times \mathbf{G}$ and $\mathbf{m} = \mathbf{n} \times \mathbf{g}$, respectively [2,93]. We now find expressions for these forces and generalized forces, by comparing the virtual work principle, Eq. (19), to the energy variation, Eq. (A7).

On the one hand, by comparing the infinitesimal variation in the position, \mathbf{u} , we find the force equilibrium equations within the bulk and on the domain boundary,

$$\mathbf{F} = \nabla \cdot \mathbf{T} \quad \text{and} \quad \mathbf{f} = \mathbf{v} \cdot \mathbf{T} + \nabla_s \cdot \mathbf{T}_s, \quad (\text{A10a,b})$$

respectively. Thus, \mathbf{T} is the stress tensor within the LC (called the Ericksen elastic stress) and \mathbf{T}_s is an additional stress vector defined on the LC boundary.

On the other hand, by comparing the infinitesimal variation in the director field, \mathbf{r} , we find the generalized force equilibrium equations within the bulk and on the domain boundary,

$$\mathbf{G} = \mathbf{h} + \lambda \mathbf{n} \quad \text{and} \quad \mathbf{g} = \mathbf{h}_s + \mu \mathbf{n}, \quad (\text{A11a,b})$$

respectively. It follows that $\mathbf{M} = \mathbf{n} \times \mathbf{h}$ is the moment vector acting on the fluid by the LC and $\mathbf{m} = \mathbf{n} \times \mathbf{h}_s$ is the couple moment vector acting on the domain boundary by the LC.

The final integral in Eq. (A7) is a line integral after applying the divergence theorem. By the principle of virtual work, this gives rise to point forces at sharp edges. These point forces shall not be discussed here further, but the reader is pointed to Ref. [46] for more information.

c. Conservative body forces

Consider the simplification of a conservative body force, that is $\mathbf{F} = -\partial\Psi/\partial\mathbf{x}$ and $\mathbf{G} = -\partial\Psi/\partial\mathbf{n}$ for some energy density function $\Psi(\mathbf{x}, \mathbf{n})$. (Here the trivial case, $\Psi = 0$, corresponds to no external forcing.) The bulk equilibrium equations, (A10a) and (A11a), take the form

$$\frac{\partial\Psi}{\partial\mathbf{x}} - \frac{\partial p}{\partial\mathbf{x}} - \nabla \cdot \left(\frac{\partial\mathcal{F}}{\partial\nabla\mathbf{n}} \cdot \nabla\mathbf{n}^T \right) = \mathbf{0} \quad \text{and} \quad \frac{\partial\Psi}{\partial\mathbf{n}} + \nabla \cdot \frac{\partial\mathcal{F}}{\partial\nabla\mathbf{n}} - \frac{\partial\mathcal{F}}{\partial\mathbf{n}} - \lambda\mathbf{n} = \mathbf{0}, \quad (\text{A12a,b})$$

respectively. Defining the total derivative as $d\mathbf{x} := \partial\mathbf{x} + \nabla\mathbf{n} \cdot \partial\mathbf{n} + \nabla(\nabla\mathbf{n}) : \partial\nabla\mathbf{n}$, we find that

$$\frac{d}{d\mathbf{x}}(\Psi - p - \mathcal{F}) = \frac{\partial}{\partial\mathbf{x}}(\Psi - p) + \nabla\mathbf{n} \cdot \frac{\partial}{\partial\mathbf{n}}(\Psi - \mathcal{F}) - \nabla(\nabla\mathbf{n}) : \frac{\partial\mathcal{F}}{\partial\nabla\mathbf{n}} = \lambda\nabla\mathbf{n} \cdot \mathbf{n} = \mathbf{0}, \quad (\text{A13})$$

where we have used Eq. (A12) and $\mathbf{n} \cdot \nabla\mathbf{n} = 0$, which follows from $\mathbf{n} \cdot \mathbf{n} = 1$. Integrating this with respect to \mathbf{x} yields the pressure $p = \Psi - \mathcal{F} + p_0$, up to an additive constant p_0 .

2. Q-tensor theory

We now derive the equilibrium forces and torques associated with a nematic LC described by a symmetric and traceless tensor $\mathbf{Q}(\mathbf{x})$, with spatial position \mathbf{x} . The net energy of the system is assumed to take the form

$$\mathcal{E} = \int_{\Omega} \mathcal{F}(\mathbf{Q}, \nabla\mathbf{Q}) - \boldsymbol{\Lambda} : \mathbf{Q} dV + \int_{\partial\Omega} \mathcal{F}_s(\mathbf{Q}; \mathbf{v}, \boldsymbol{\tau}) - \boldsymbol{\mu} : \mathbf{Q} dA, \quad (\text{A14})$$

for the bulk energy density \mathcal{F} , e.g., Eqs. (2) and (3); surface energy density \mathcal{F}_s , e.g., Rapini-Papoular, Eq. (17), or Fournier-Galatola, Eq. (18); and $\Lambda_{ij} = \lambda\delta_{ij} + \lambda_k\epsilon_{ijk}$ and $\mu_{ij} = \mu\delta_{ij} + \mu_k\epsilon_{ijk}$ (where repeated indices indicate summation, and δ_{ij} and ϵ_{ijk} are the components of the Kronecker delta and

Levi-Civita tensor), for the eight Lagrange multipliers λ , λ_k , μ , and μ_k that impose the symmetries $\text{Tr}(\mathbf{Q}) = 0$ and $\mathbf{Q}^T = \mathbf{Q}$.

a. Energy variation

Analogous to the variational principle presented in Sec. A 1 for the theory based on the director field \mathbf{n} , the energy here may be reduced by either varying the spatial position, $\tilde{\mathbf{x}} = \mathbf{x} + \mathbf{u}(\mathbf{x})$, with displacement vector $\mathbf{u} := \delta\mathbf{x}$, or the alignment tensor, $\tilde{\mathbf{Q}}(\tilde{\mathbf{x}}) = \mathbf{Q}(\mathbf{x}) + \mathbf{R}(\mathbf{x})$, with Eulerian variation $\mathbf{R} := \Delta\mathbf{Q} = \delta\mathbf{Q} + \delta\mathbf{x} \cdot \nabla\mathbf{Q}$. Using the variation identities in Eqs. (A2)–(A4), one can show that the functional derivative of the energy is

$$\delta\mathcal{E} = \int_{\Omega} \delta\mathcal{F} - \mathbf{\Lambda} : \mathbf{R} - p(\nabla \cdot \mathbf{u}) dV + \int_{\partial\Omega} \delta\mathcal{F}_s + \mathcal{F}_s(\mathbf{P}(\mathbf{v}) : \nabla_s \mathbf{u}) - \boldsymbol{\mu} : \mathbf{R} dA, \quad (\text{A15})$$

where p is the Lagrange multiplier imposing incompressibility,

$$\delta\mathcal{F} = \mathbf{R} : \frac{\partial\mathcal{F}}{\partial\mathbf{Q}} + (\nabla\mathbf{R} - \nabla\mathbf{u} \cdot \nabla\mathbf{Q}) : \frac{\partial\mathcal{F}}{\partial\nabla\mathbf{Q}}, \quad (\text{A16a})$$

$$\text{and } \delta\mathcal{F}_s = \mathbf{R} : \frac{\partial\mathcal{F}_s}{\partial\mathbf{Q}} - (\nabla_s \mathbf{u} \cdot \mathbf{v}) \cdot \frac{\partial\mathcal{F}_s}{\partial\mathbf{v}} + (\boldsymbol{\tau} \cdot \nabla_s \mathbf{u} \cdot \mathbf{P}(\boldsymbol{\tau})) \cdot \frac{\partial\mathcal{F}_s}{\partial\boldsymbol{\tau}}. \quad (\text{A16b})$$

Integrating by parts yields

$$\begin{aligned} \delta\mathcal{E} = & - \int_{\Omega} (\mathbf{H} + \mathbf{\Lambda}) : \mathbf{R} + (\nabla \cdot \mathbf{T}) \cdot \mathbf{u} dV - \int_{\partial\Omega} (\mathbf{H}_s + \boldsymbol{\mu}) : \mathbf{R} + (\mathbf{v} \cdot \mathbf{T} + \nabla_s \cdot \mathbf{T}_s) \cdot \mathbf{u} dA \\ & + \int_{\partial\Omega} \nabla_s \cdot (\mathbf{T}_s \cdot \mathbf{u}) dA, \end{aligned} \quad (\text{A17})$$

for the bulk and surface molecular field tensors, \mathbf{H} and \mathbf{H}_s , defined in Eq. (14), and the bulk and surface stress tensors, \mathbf{T} and \mathbf{T}_s , defined in Eqs. (25) and (21b), respectively.

b. Principle of virtual work

At equilibrium, the energy variation satisfies the principle of virtual work,

$$\delta\mathcal{E} = - \int_{\Omega} \mathbf{F} \cdot \mathbf{u} + \mathbf{G} : \mathbf{R} dV - \int_{\partial\Omega} \mathbf{f} \cdot \mathbf{u} + \mathbf{g} : \mathbf{R} dA, \quad (\text{A18})$$

for the force acting on the bulk \mathbf{F} , force acting on the boundary \mathbf{f} , generalized force acting on the bulk \mathbf{G} , and generalized force acting on the boundary \mathbf{g} . Here the generalized forces are second-order tensors (in contrast to in Sec. A 1, where they were vectors). These can again be related to the moment vectors acting on the bulk and the boundary, \mathbf{M} and \mathbf{m} , respectively, by considering an arbitrary infinitesimal rigid rotation $\boldsymbol{\omega}$. Here $\mathbf{u} = \boldsymbol{\omega} \times \mathbf{x}$ and $R_{ij} = \omega_k (\epsilon_{ikl} Q_{lj} + \epsilon_{jkl} Q_{il})$, where repeated indices imply summation and ϵ_{ikl} is the Levi-Civita symbol. Inserting these into Eq. (A18) and rearranging yields, at equilibrium, the conservation of angular momentum

$$\delta\mathcal{E} = -\boldsymbol{\omega} \cdot \left(\int_{\Omega} \mathbf{x} \times \mathbf{F} + \mathbf{M} dV + \int_{\partial\Omega} \mathbf{x} \times \mathbf{f} + \mathbf{m} dA \right), \quad (\text{A19})$$

for $\mathbf{M}_i = \epsilon_{ijk} (\mathbf{Q} \cdot \mathbf{G} - \mathbf{G} \cdot \mathbf{Q})_{jk}$ and $\mathbf{m}_i = \epsilon_{ijk} (\mathbf{Q} \cdot \mathbf{g} - \mathbf{g} \cdot \mathbf{Q})_{jk}$, see, e.g., Ref. [95] for further details.

By comparing the energy variations, Eqs. (A17) and (A18), we find the force and generalized force equilibrium equations,

$$\mathbf{F} = \nabla \cdot \mathbf{T}, \quad \mathbf{f} = \mathbf{v} \cdot \mathbf{T} + \nabla_s \cdot \mathbf{T}_s, \quad \mathbf{G} = \mathbf{H} + \mathbf{\Lambda}, \quad \mathbf{g} = \mathbf{H}_s + \boldsymbol{\mu}. \quad (\text{A20a–d})$$

It follows that the moment acting on the fluid and on the domain boundary by the LC are those given in Eq. (27).

c. Conservative body forces

Consider again the simplification of a conservative body force, that is $\mathbf{F} = -\partial\Psi/\partial\mathbf{x}$ and $\mathbf{G} = -\partial\Psi/\partial\mathbf{Q}$ for some energy density function $\Psi(\mathbf{x}, \mathbf{Q})$. Here the bulk equilibrium equations take the form

$$\frac{\partial\Psi}{\partial\mathbf{x}} - \frac{\partial p}{\partial\mathbf{x}} - \nabla \cdot \left(\frac{\partial\mathcal{F}}{\partial\nabla\mathbf{Q}} : \nabla\mathbf{Q}^T \right) = \mathbf{0} \quad \text{and} \quad \frac{\partial\Psi}{\partial\mathbf{Q}} + \nabla \cdot \frac{\partial\mathcal{F}}{\partial\nabla\mathbf{Q}} - \frac{\partial\mathcal{F}}{\partial\mathbf{Q}} - \mathbf{\Lambda} = \mathbf{0}. \quad (\text{A21a,b})$$

Defining the total derivative as $d\mathbf{x} := \partial\mathbf{x} + \nabla\mathbf{Q} : \partial\mathbf{Q} + \nabla(\nabla\mathbf{Q}) : \partial\nabla\mathbf{Q}$, we have that

$$\frac{d}{d\mathbf{x}}(\Psi - p - \mathcal{F}) = \frac{\partial}{\partial\mathbf{x}}(\Psi - p) + \nabla\mathbf{Q} : \frac{\partial}{\partial\mathbf{Q}}(\Psi - \mathcal{F}) - \nabla(\nabla\mathbf{Q}) : \frac{\partial\mathcal{F}}{\partial\nabla\mathbf{Q}} = \nabla\mathbf{Q} : \mathbf{\Lambda} = \mathbf{0}, \quad (\text{A22})$$

after imposing Eq. (A21) and the symmetries of \mathbf{Q} , i.e., $\text{Tr}(\mathbf{Q}) = 0$ and $\mathbf{Q}^T = \mathbf{Q}$. As before, it follows that $p = \Psi - \mathcal{F} + p_0$.

-
- [1] T. Sluckin, D. Dunmur, and H. Stegemeyer, *Crystals that Flow* (Taylor & Francis, London, 2004).
 - [2] P.-G. de Gennes and J. Prost, *The Physics of Liquid Crystals* (Oxford University Press, Oxford, 1993).
 - [3] S. Zhou, K. Neupane, Y. Nastishin, A. Baldwin, S. Shiyakovskii, O. Lavrentovich, and S. Sprunt, Elasticity, viscosity, and oriental fluctuations of a lyotropic chromonic nematic liquid crystal disodium cromoglycate, *Soft Matter* **10**, 6571 (2014).
 - [4] H. Kawamoto, The history of liquid-crystal displays, *Proc. IEEE* **90**, 460 (2002).
 - [5] D. Tampion and R. A. Gibbons, Orientation of spermatozoa in mucus of the cervix uteri, *Nature (Lond.)* **194**, 381 (1962).
 - [6] C. Viney, A. E. Huber, and P. Verdugo, Liquid-crystalline order in mucus, *Macromolecules* **26**, 852 (1993).
 - [7] I. I. Smalyukh, J. Butler, J. D. ShROUT, M. R. Parsek, and G. C. L. Wong, Elasticity-mediated nematiclike bacterial organization in model extracellular DNA matrix, *Phys. Rev. E* **78**, 030701(R) (2008).
 - [8] H.-C. Flemming and J. Wingender, The biofilm matrix, *Nature Rev. Microbiol.* **8**, 623 (2010).
 - [9] R. Hartmann, P. K. Singh, P. Pearce, R. Mok, B. Song, F. Díaz-Pascual, J. Dunkel, and K. Drescher, Emergence of three-dimensional order and structure in growing biofilms, *Nat. Phys.* **15**, 251 (2019).
 - [10] J. Nijjer, C. Li, M. Kothari, T. Henzel, Q. Zhang, J.-S. B. Tai, S. Zhou, T. Cohen, S. Zhang, and J. Yan, Biofilms as self-shaping growing nematics, *Nat. Phys.* **19**, 1936 (2023).
 - [11] P. C. Mushenheim, R. R. Trivedi, H. H. Tuson, D. B. Weibel, and N. L. Abbott, Dynamic self-assembly of motile bacteria in liquid crystals, *Soft Matter* **10**, 88 (2014).
 - [12] S. Zhou, A. Sokolov, O. D. Lavrentovich, and I. S. Aranson, Living liquid crystals, *Proc. Natl. Acad. Sci. USA* **111**, 1265 (2014).
 - [13] R. R. Trivedi, R. Maeda, N. L. Abbott, S. E. Spagnolie, and D. B. Weibel, Bacterial transport of colloids in liquid crystalline environments, *Soft Matter* **11**, 8404 (2015).
 - [14] N. Figueroa-Morales, L. Dominguez-Rubio, T. L. Ott, and I. S. Aranson, Mechanical shear controls bacterial penetration in mucus, *Sci. Rep.* **9**, 9713 (2019).
 - [15] M. Goral, E. Clement, T. Darnige, T. Lopez-Leon, and A. Lindner, Frustrated “run and tumble” of swimming *Escherichia coli* bacteria in nematic liquid crystals, *Interface Focus* **12**, 20220039 (2022).
 - [16] A. G. Prabhune, A. S. García-Gordillo, I. S. Aranson, T. R. Powers, and N. Figueroa-Morales, Bacteria navigate anisotropic media using a flagellar Tug-of-Oars, *PRX Life* **2**, 033004 (2024).
 - [17] D. Volfson, S. Cookson, J. Hasty, and L. S. Tsimring, Biomechanical ordering of dense cell populations, *Proc. Natl. Acad. Sci. USA* **105**, 15346 (2008).
 - [18] D. Dell’Arciprete, M. L. Blow, A. T. Brown, F. D. C. Farrell, J. S. Lintuvuori, A. F. McVey, D. Marenduzzo, and W. C. K. Poon, A growing bacterial colony in two dimensions as an active nematic, *Nat. Commun.* **9**, 4190 (2018).

- [19] Y. I. Yaman, E. Demir, R. Vetter, and A. Kocabas, Emergence of active nematics in chaining bacterial biofilms, *Nat. Commun.* **10**, 2285 (2019).
- [20] K. Copenhagen, R. Alert, N. S. Wingreen, and J. W. Shaevitz, Topological defects promote layer formation in *Myxococcus xanthus* colonies, *Nat. Phys.* **17**, 211 (2021).
- [21] M. J. Shelley, The dynamics of microtubule/motor-protein assemblies in biology and physics, *Annu. Rev. Fluid Mech.* **48**, 487 (2016).
- [22] D. Needleman and Z. Dogic, Active matter at the interface between materials science and cell biology, *Nature Rev. Mat.* **2**, 17048 (2017).
- [23] Y. Maroudas-Sacks, L. Garion, L. Shani-Zerbib, A. Livshits, E. Braun, and K. Keren, Topological defects in the nematic order of actin fibres as organization centres of hydra morphogenesis, *Nat. Phys.* **17**, 251 (2021).
- [24] W. Mirza, M. De Corato, M. Pensalfini, G. Vilanova, A. Torres-Sánchez, and M. Arroyo, Theory of active self-organization of dense nematic structures in the actin cytoskeleton, *eLife* **13**, RP93097 (2024).
- [25] R. Bruinsma, A. Y. Grosberg, Y. Rabin, and A. Zidovska, Chromatin hydrodynamics, *Biophys. J.* **106**, 1871 (2014).
- [26] A. Mahajan, W. Yan, A. Zidovska, D. Saintillan, and M. J. Shelley, Euchromatin activity enhances segregation and compaction of heterochromatin in the cell nucleus, *Phys. Rev. X* **12**, 041033 (2022).
- [27] I. Eshghi, A. Zidovska, and A. Y. Grosberg, Activity-driven phase transition causes coherent flows of chromatin, *Phys. Rev. Lett.* **131**, 048401 (2023).
- [28] M. C. Marchetti, J. F. Joanny, S. Ramaswamy, T. B. Liverpool, J. Prost, M. Rao, and R. A. Simha, Hydrodynamics of soft active matter, *Rev. Mod. Phys.* **85**, 1143 (2013).
- [29] D. Saintillan and M. J. Shelley, Theory of active suspensions, in *Complex Fluids in Biological Systems* (Springer, Berlin, 2015), pp. 319–351.
- [30] A. Doostmohammadi, J. Ignés-Mullol, J. M. Yeomans, and F. Sagués, Active nematics, *Nat. Commun.* **9**, 3246 (2018).
- [31] T. Hegmann, H. Qi, and V. M. Marx, Nanoparticles in liquid crystals: Synthesis, self-assembly, defect formation and potential applications, *J. Inorg. Organomet. Polym. Mater.* **17**, 483 (2007).
- [32] Y. Shen and I. Dierking, Perspectives in liquid-crystal-aided nanotechnology and nanoscience, *Appl. Sci.* **9**, 2512 (2019).
- [33] Y.-K. Kim, J. Noh, K. Nayani, and N. L. Abbott, Soft matter from liquid crystals, *Soft Matter* **15**, 6913 (2019).
- [34] T. C. Lubensky, D. Pettey, N. Currier, and H. Stark, Topological defects and interactions in nematic emulsions, *Phys. Rev. E* **57**, 610 (1998).
- [35] G. P. Alexander, B. G. Chen, E. A. Matsumoto, and R. D. Kamien, Colloquium: Disclination loops, point defects, and all that in nematic liquid crystals, *Rev. Mod. Phys.* **84**, 497 (2012).
- [36] D. Dunmur and T. Sluckin, *Soap, Science, and Flat-Screen TVs: A History of Liquid Crystals* (Oxford University Press, Oxford, 2014).
- [37] B. Jerome, Surface effects and anchoring in liquid crystals, *Rep. Prog. Phys.* **54**, 391 (1991).
- [38] P. Prinsen and P. van der Schoot, Shape and director-field transformation of tactoids, *Phys. Rev. E* **68**, 021701 (2003).
- [39] P. C. Mushenheim, J. S. Pendery, D. B. Weibel, S. E. Spagnolie, and N. L. Abbott, Straining soft colloids in aqueous nematic liquid crystals, *Proc. Natl. Acad. Sci. USA* **113**, 5564 (2016).
- [40] R. Zhang, Y. Zhou, J. A. Martínez-González, J. P. Hernández-Ortiz, N. L. Abbott, and J. J. De Pablo, Controlled deformation of vesicles by flexible structured media, *Sci. Adv.* **2**, e1600978 (2016).
- [41] P. Jani, K. Nayani, and N. L. Abbott, Sculpting the shapes of giant unilamellar vesicles using isotropic–nematic–isotropic phase cycles, *Soft Matter* **17**, 9078 (2021).
- [42] K. Nayani, A. A. Evans, S. E. Spagnolie, and N. L. Abbott, Dynamic and reversible shape response of red blood cells in synthetic liquid crystals, *Proc. Natl. Acad. Sci. USA* **117**, 26083 (2020).
- [43] M. Kleman and O. D. Lavrentovich, *Soft Matter Physics: An Introduction* (Springer, Berlin, 2003).
- [44] J. V. Selinger, Interpretation of saddle-splay and the Oseen-Frank free energy in liquid crystals, *Liquid Cryst. Rev.* **6**, 129 (2018).
- [45] J. L. Ericksen, Inequalities in liquid crystal theory, *Phys. Fluids* **9**, 1205 (1966).

- [46] E. G. Virga, *Variational Theories for Liquid Crystals* (Chapman & Hall/CRC, Boca Raton, FL, 2018).
- [47] N. M. Silvestre, P. Patrício, and M. M. Telo da Gama, Elliptical soft colloids in smectic-C films, *Phys. Rev. E* **74**, 021706 (2006).
- [48] P. V. Dolganov, H. T. Nguyen, G. Joly, V. K. Dolganov, and P. Cluzeau, Shape of nematic droplets in smectic membranes, *Europhys. Lett.* **78**, 66001 (2007).
- [49] C. Bohley and R. Stannarius, Inclusions in free standing smectic liquid crystal films, *Soft Matter* **4**, 683 (2008).
- [50] U. Tkalec and I. Mušević, Topology of nematic liquid crystal colloids confined to two dimensions, *Soft Matter* **9**, 8140 (2013).
- [51] A. H. Lewis, I. Garlea, J. Alvarado, O. J. Dammeone, P. D. Howell, A. Majumdar, B. M. Mulder, M. P. Lettinga, G. H. Koenderink, and D. G. A. L. Aarts, Colloidal liquid crystals in rectangular confinement: Theory and experiment, *Soft Matter* **10**, 7865 (2014).
- [52] T. M. Fischer, R. F. Bruinsma, and C. M. Knobler, Textures of surfactant monolayers, *Phys. Rev. E* **50**, 413 (1994).
- [53] D. K. Schwartz, M.-W. Tsao, and C. M. Knobler, Domain morphology in a two-dimensional anisotropic mesophase: Cusps and boojum textures in a Langmuir monolayer, *J. Chem. Phys.* **101**, 8258 (1994).
- [54] D. Pettey and T. C. Lubensky, Stability of texture and shape of circular domains of Langmuir monolayers, *Phys. Rev. E* **59**, 1834 (1999).
- [55] M. Kléman, Defects in liquid crystals, *Rep. Prog. Phys.* **52**, 555 (1989).
- [56] F.-H. Lin and C. Liu, Existence of solutions for the Ericksen-Leslie system, *Arch. Ration. Mech. Anal.* **154**, 135 (2000).
- [57] C. Liu and N. J. Walkington, Approximation of liquid crystal flows, *SIAM J. Numer. Anal.* **37**, 725 (2000).
- [58] S. Hess, Fokker-Planck-equation approach to flow alignment in liquid crystals, *Zeitschr. Naturforsch. A* **31**, 1034 (1976).
- [59] M. Ravnik and S. Žumer, Landau–de Gennes modelling of nematic liquid crystal colloids, *Liq. Cryst.* **36**, 1201 (2009).
- [60] N. J. Mottram and C. J. P. Newton, Introduction to Q-tensor theory, [arXiv:1409.3542](https://arxiv.org/abs/1409.3542).
- [61] J. Katriel, G. F. Kventsel, G. R. Luckhurst, and T. J. Sluckin, Free energies in the Landau and molecular field approaches, *Liq. Cryst.* **1**, 337 (1986).
- [62] J. M. Ball, Mathematics and liquid crystals, *Mol. Cryst. Liq. Cryst.* **647**, 1 (2017).
- [63] J. L. Ericksen, Liquid crystals with variable degree of orientation, *Arch. Ration. Mech. Anal.* **113**, 97 (1991).
- [64] M. Doi and S. F. Edwards, *The Theory of Polymer Dynamics* (Oxford University Press, Oxford, UK, 1988).
- [65] A. N. Beris and B. J. Edwards, *Thermodynamics of Flowing Systems: With Internal Microstructure* (Oxford University Press, Oxford, 1994).
- [66] J. P. Hernández-Ortiz, B. T. Gettelfinger, J. Moreno-Razo, and J. J. de Pablo, Modeling flows of confined nematic liquid crystals, *J. Chem. Phys.* **134**, 134905 (2011).
- [67] L. Longa, D. Monselesan, and H.-R. Trebin, An extension of the Landau-Ginzburg-de Gennes theory for liquid crystals, *Liq. Cryst.* **2**, 769 (1987).
- [68] J. P. Borthagaray and S. W. Walker, The Q-tensor model with uniaxial constraint, in *Handbook on Numerical Analysis*, Vol. 22 (Elsevier, Amsterdam, 2021), pp. 313–382.
- [69] Q. Li, *Liquid Crystals Beyond Displays: Chemistry, Physics, and Applications* (John Wiley & Sons, New York, 2012).
- [70] M. Škarabot, M. Ravnik, S. Žumer, U. Tkalec, I. Poberaj, D. Babic, N. Osterman, and I. Musevic, Two-dimensional dipolar nematic colloidal crystals, *Phys. Rev. E* **76**, 051406 (2007).
- [71] Y. Gu and N. L. Abbott, Observation of Saturn-ring defects around solid microspheres in nematic liquid crystals, *Phys. Rev. Lett.* **85**, 4719 (2000).
- [72] C. P. Lapointe, T. G. Mason, and I. I. Smalyukh, Shape-controlled colloidal interactions in nematic liquid crystals, *Science* **326**, 1083 (2009).
- [73] H. Stark, Physics of colloidal dispersions in nematic liquid crystals, *Phys. Rep.* **351**, 387 (2001).

- [74] I. Mušević, Nematic liquid-crystal colloids, *Materials* **11**, 24 (2017).
- [75] I. Musevic, *Liquid Crystal Colloids* (Springer, Berlin, 2017).
- [76] I. I. Smalyukh, Liquid crystal colloids, *Annu. Rev. Condens. Matter Phys.* **9**, 207 (2018).
- [77] O. D. Lavrentovich, Transport of particles in liquid crystals, *Soft Matter* **10**, 1264 (2014).
- [78] B.-K. Lee, S.-J. Kim, B. Lev, and J.-H. Kim, Motion of a colloidal particle in a nonuniform director field of a nematic liquid crystal, *Phys. Rev. E* **95**, 012709 (2017).
- [79] E. M. Terentjev, Disclination loops, standing alone and around solid particles, in nematic liquid crystals, *Phys. Rev. E* **51**, 1330 (1995).
- [80] O. D. Lavrentovich, Topological defects in dispersed words and worlds around liquid crystals, or liquid crystal drops, *Liq. Cryst.* **24**, 117 (1998).
- [81] H. Stark, Director field configurations around a spherical particle in a nematic liquid crystal, *Eur. Phys. J. B* **10**, 311 (1999).
- [82] J. S. Lintuvuori, K. Stratford, M. E. Cates, and D. Marenduzzo, Colloids in cholesterics: Size-dependent defects and non-Stokesian microrheology, *Phys. Rev. Lett.* **105**, 178302 (2010).
- [83] G. E. Volovik and O. D. Lavrentovich, Topological dynamics of defects: Boojums in nematic drops, *Zh. Exp. Teor. Fiz.* **85**, 1997 (1983).
- [84] T. G. J. Chandler and S. E. Spagnolie, A nematic liquid crystal with an immersed body: Equilibrium, stress and paradox, *J. Fluid Mech.* **967**, A19 (2023).
- [85] P. Poulin and D. A. Weitz, Inverted and multiple nematic emulsions, *Phys. Rev. E* **57**, 626 (1998).
- [86] R. D. Williams, Two transitions in tangentially anchored nematic droplets, *J. Phys. A: Math. Gen.* **19**, 3211 (1986).
- [87] P. Prinsen and P. Van der Schoot, Parity breaking in nematic tactoids, *J. Phys.: Condens. Matter* **16**, 8835 (2004).
- [88] L. Tortora and O. D. Lavrentovich, Chiral symmetry breaking by spatial confinement in tactoidal droplets of lyotropic chromonic liquid crystals, *Proc. Natl. Acad. Sci. USA* **108**, 5163 (2011).
- [89] J. L. Ericksen, Hydrostatic theory of liquid crystals, *Arch. Ration. Mech. Anal.* **9**, 371 (1962).
- [90] A. Rapini and M. Papoular, Distorsion d'une lamelle nématique sous champ magnétique conditions d'ancrage aux parois, *J. Phys. Colloq.* **30**, C4-54 (1969).
- [91] G. Barbero and G. Durand, On the validity of the Rapini-Papoular surface anchoring energy form in nematic liquid crystals, *J. Phys. France* **47**, 2129 (1986).
- [92] J. T. Jenkins and P. J. Barratt, Interfacial effects in the static theory of nematic liquid crystals, *Q. J. Mech. Appl. Math.* **27**, 111 (1974).
- [93] I. W. Stewart, *The Static and Dynamic Continuum Theory of Liquid Crystals: A Mathematical Introduction* (CRC Press, Boca Raton, FL, 2004).
- [94] A. M. Sonnet and E. G. Virga, *Dissipative Ordered Fluids: Theories for Liquid Crystals*, Vol. 100 (Springer Science & Business Media, New York, 2012).
- [95] T. Qian and P. Sheng, Generalized hydrodynamic equations for nematic liquid crystals, *Phys. Rev. E* **58**, 7475 (1998).
- [96] E. Willman, F. A. Fernández, R. James, and S. E. Day, Modeling of weak anisotropic anchoring of nematic liquid crystals in the Landau–de Gennes theory, *IEEE Trans. Electr. Devices* **54**, 2630 (2007).
- [97] M. Nobili and G. Durand, Disorientation-induced disordering at a nematic-liquid-crystal–solid interface, *Phys. Rev. A* **46**, R6174 (1992).
- [98] J.-B. Fournier and P. Galatola, Modeling planar degenerate wetting and anchoring in nematic liquid crystals, *Europhys. Lett.* **72**, 403 (2005).
- [99] N. Kuzuu and M. Doi, Constitutive equation for nematic liquid crystals under weak velocity gradient derived from a molecular kinetic equation, *J. Phys. Soc. Jpn.* **52**, 3486 (1983).
- [100] J. Han, Y. Luo, W. Wang, P. Zhang, and Z. Zhang, From microscopic theory to macroscopic theory: A systematic study on modeling for liquid crystals, *Arch. Ration. Mech. Anal.* **215**, 741 (2015).
- [101] W. Wang, P. Zhang, and Z. Zhang, Rigorous derivation from Landau–de Gennes theory to Ericksen–Leslie theory, *SIAM J. Math. Anal.* **47**, 127 (2015).
- [102] E. C. Gartland Jr., Forces and variational compatibility for equilibrium liquid crystal director models with coupled electric fields, *Contin. Mech. Thermodyn.* **32**, 1559 (2020).

- [103] M. M. Müller, M. Deserno, and J. Guven, Geometry of surface-mediated interactions, *Europhys. Lett.* **69**, 482 (2005).
- [104] R. W. Style, Y. Che, S. J. Park, B. M. Weon, J. H. Je, C. Hyland, G. K. German, M. P. Power, L. A. Wilen, J. S. Wettlaufer *et al.*, Patterning droplets with durotaxis, *Proc. Natl. Acad. Sci. USA* **110**, 12541 (2013).
- [105] R. W. Style, A. Jagota, C.-Y. Hui, and E. R. Dufresne, Elastocapillarity: Surface tension and the mechanics of soft solids, *Annu. Rev. Condens. Matt. Phys.* **8**, 99 (2017).
- [106] J. Bico, É. Reyssat, and B. Roman, Elastocapillarity: When surface tension deforms elastic solids, *Annu. Rev. Fluid Mech.* **50**, 629 (2018).
- [107] D. Vella and L. Mahadevan, The “Cheerios effect,” *Am. J. Phys.* **73**, 817 (2005).
- [108] L. Botto, E. P. Lewandowski, M. Cavallaro, and K. J. Stebe, Capillary interactions between anisotropic particles, *Soft Matter* **8**, 9957 (2012).
- [109] I. B. Liu, N. Sharifi-Mood, and K. J. Stebe, Capillary assembly of colloids: Interactions on planar and curved interfaces, *Annu. Rev. Condens. Matter Phys.* **9**, 283 (2018).
- [110] P. Poulin, H. Stark, T. C. Lubensky, and D. A. Weitz, Novel colloidal interactions in anisotropic fluids, *Science* **275**, 1770 (1997).
- [111] D. Andrienko, M. Tasinkevych, P. Patricio, M. P. Allen, and M. M. Telo da Gama, Forces between elongated particles in a nematic colloid, *Phys. Rev. E* **68**, 051702 (2003).
- [112] D. L. Cheung and M. P. Allen, Forces between cylindrical nanoparticles in a liquid crystal, *Langmuir* **24**, 1411 (2008).
- [113] P. Poulin, N. Francès, and O. Mondain-Monval, Suspension of spherical particles in nematic solutions of disks and rods, *Phys. Rev. E* **59**, 4384 (1999).
- [114] J.-C. Loudet, P. Barois, and P. Poulin, Colloidal ordering from phase separation in a liquid-crystalline continuous phase, *Nature (Lond.)* **407**, 611 (2000).
- [115] I. I. Smalyukh, O. D. Lavrentovich, A. N. Kuzmin, A. V. Kachynski, and P. N. Prasad, Elasticity-mediated self-organization and colloidal interactions of solid spheres with tangential anchoring in a nematic liquid crystal, *Phys. Rev. Lett.* **95**, 157801 (2005).
- [116] S. B. Chernyshuk, High-order elastic terms, boojums and general paradigm of the elastic interaction between colloidal particles in the nematic liquid crystals, *Eur. Phys. J. E* **37**, 6 (2014).
- [117] F. Mondiot, R. Botet, P. Snabre, O. Mondain-Monval, and J.-C. Loudet, Colloidal aggregation and dynamics in anisotropic fluids, *Proc. Natl. Acad. Sci.* **111**, 5831 (2014).
- [118] V. G. Nazarenko, A. B. Nych, and B. I. Lev, Crystal structure in nematic emulsion, *Phys. Rev. Lett.* **87**, 075504 (2001).
- [119] M. Škarabot, M. Ravnik, S. Žumer, U. Tkalec, I. Poberaj, D. Babic, N. Osterman, and I. Musevic, Interactions of quadrupolar nematic colloids, *Phys. Rev. E* **77**, 031705 (2008).
- [120] O. Guzmán, E. B. Kim, S. Grollau, N. L. Abbott, and J. J. de Pablo, Defect structure around two colloids in a liquid crystal, *Phys. Rev. Lett.* **91**, 235507 (2003).
- [121] V. Tomar, T. F. Roberts, N. L. Abbott, J. P. Hernández-Ortiz, and J. J. De Pablo, Liquid crystal mediated interactions between nanoparticles in a nematic phase, *Langmuir* **28**, 6124 (2012).
- [122] Y. Wang, P. Zhang, and J. Z. Y. Chen, Topological defects in an unconfined nematic fluid induced by single and double spherical colloidal particles, *Phys. Rev. E* **96**, 042702 (2017).
- [123] U. Tkalec, M. Ravnik, S. Čopar, S. Žumer, and I. Mušević, Reconfigurable knots and links in chiral nematic colloids, *Science* **333**, 62 (2011).
- [124] M. Ravnik, M. Škarabot, S. Žumer, U. Tkalec, I. Poberaj, D. Babič, N. Osterman, and I. Mušević, Entangled nematic colloidal dimers and wires, *Phys. Rev. Lett.* **99**, 247801 (2007).
- [125] M. Ravnik and S. Žumer, Nematic colloids entangled by topological defects, *Soft Matter* **5**, 269 (2009).
- [126] F. R. Hung, O. Guzmán, B. T. Gettelfinger, N. L. Abbott, and J. J. de Pablo, Anisotropic nanoparticles immersed in a nematic liquid crystal: Defect structures and potentials of mean force, *Phys. Rev. E* **74**, 011711 (2006).
- [127] A. Nych, U. Ognysta, M. Skarabot, M. Ravnik, S. Žumer, and I. Musevic, Assembly and control of 3D nematic dipolar colloidal crystals, *Nat. Commun.* **4**, 1489 (2013).

- [128] M. A. Gharbi, M. Cavallaro, Jr., G. Wu, D. A. Beller, R. D. Kamien, S. Yang, and K. J. Stebe, Microbullet assembly: interactions of oriented dipoles in confined nematic liquid crystal, *Liq. Cryst.* **40**, 1619 (2013).
- [129] M. Tasinkevych, F. Mondiot, O. Mondain-Monval, and J.-C. Loudet, Dispersions of ellipsoidal particles in a nematic liquid crystal, *Soft Matter* **10**, 2047 (2014).
- [130] F. Mondiot, S. P. Chandran, O. Mondain-Monval, and J.-C. Loudet, Shape-induced dispersion of colloids in anisotropic fluids, *Phys. Rev. Lett.* **103**, 238303 (2009).
- [131] X. Fan and A. Walther, 1D Colloidal chains: Recent progress from formation to emergent properties and applications, *Chem. Soc. Rev.* **51**, 4023 (2022).
- [132] N. V. Solodkov, J.-U. Shim, and J. C. Jones, Self-assembly of fractal liquid crystal colloids, *Nat. Commun.* **10**, 198 (2019).
- [133] J.-I. Fukuda, B. I. Lev, and H. Yokoyama, Effect of confining walls on the interaction between particles in a nematic liquid crystal, *J. Phys.: Condens. Matter* **15**, 3841 (2003).
- [134] S. R. Seyednejad, M. R. Mozaffari, and M. R. Ejtehadi, Confined nematic liquid crystal between two spherical boundaries with planar anchoring, *Phys. Rev. E* **88**, 012508 (2013).
- [135] I. M. Tambovtsev, I. S. Lobanov, A. D. Kiselev, and V. M. Uzdin, Pair interaction of localized topological structures in confined chiral media, *Phys. Rev. E* **108**, 024705 (2023).
- [136] S. Ramaswamy, R. Nityananda, V. A. Raghunathan, and J. Prost, Power-law forces between particles in a nematic, *Mol. Cryst. Liq. Cryst. Sci. Technol. A* **288**, 175 (1996).
- [137] R. W. Ruhwandl and E. M. Terentjev, Long-range forces and aggregation of colloid particles in a nematic liquid crystal, *Phys. Rev. E* **55**, 2958 (1997).
- [138] J.-I. Fukuda, H. Stark, M. Yoneya, and H. Yokoyama, Interaction between two spherical particles in a nematic liquid crystal, *Phys. Rev. E* **69**, 041706 (2004).
- [139] S. Alama, L. Bronsard, X. Lamy, and R. Venkatraman, Far-field expansions for harmonic maps and the electrostatics analogy in nematic suspensions, *J. Nonlin. Sci.* **33**, 39 (2023).
- [140] B. Senyuk, O. Puls, O. M. Tovkach, S. B. Chernyshuk, and I. I. Smalyukh, Hexadecapolar colloids, *Nat. Commun.* **7**, 10659 (2016).
- [141] B. I. Lev, S. B. Chernyshuk, P. M. Tomchuk, and H. Yokoyama, Symmetry breaking and interaction of colloidal particles in nematic liquid crystals, *Phys. Rev. E* **65**, 021709 (2002).
- [142] V. M. Pergamenschchik and V. O. Uzunova, Elastic charge density representation of the interaction via the nematic director field, *Eur. Phys. J. E* **23**, 161 (2007).
- [143] V. M. Pergamenschchik and V. A. Uzunova, Dipolar colloids in nematostatics: Tensorial structure, symmetry, different types, and their interaction, *Phys. Rev. E* **83**, 021701 (2011).
- [144] S. B. Chernyshuk and B. I. Lev, Elastic interaction between colloidal particles in confined nematic liquid crystals, *Phys. Rev. E* **81**, 041701 (2010).
- [145] T. Kishita, N. Kondo, K. Takahashi, M. Ichikawa, J.-I. Fukuda, and Y. Kimura, Interparticle force in nematic colloids: Comparison between experiment and theory, *Phys. Rev. E* **84**, 021704 (2011).
- [146] O. M. Tovkach, S. B. Chernyshuk, and B. I. Lev, Colloidal interactions in a homeotropic nematic cell with different elastic constants, *Phys. Rev. E* **92**, 042505 (2015).
- [147] T. G. J. Chandler and S. E. Spagnolie, Exact and approximate solutions for elastic interactions in a nematic liquid crystal, [arXiv:2311.17708](https://arxiv.org/abs/2311.17708).
- [148] A. J. H. Houston and G. P. Alexander, Colloids in two-dimensional active nematics: Conformal cogs and controllable spontaneous rotation, *New J. Phys.* **25**, 123006 (2023).
- [149] H. Miyazako and T. Sakajo, Defect pairs in nematic cell alignment on doubly connected domains, *Proc. R. Soc. A* **480**, 20230879 (2024).
- [150] D. Crowdy, *Solving Problems in Multiply Connected Domains* (SIAM, Philadelphia, 2020).
- [151] A. V. Kaznacheev, M. M. Bogdanov, and S. A. Taraskin, The nature of prolate shape of tactoids in lyotropic inorganic liquid crystals, *J. Exp. Theor. Phys.* **95**, 57 (2002).
- [152] S. Papparini and E. G. Virga, Nematic tactoid population, *Phys. Rev. E* **103**, 022707 (2021).
- [153] H. S. Ansell, D. S. Kim, R. D. Kamien, E. Katifori, and T. Lopez-Leon, Threading the spindle: A geometric study of chiral liquid crystal polymer microparticles, *Phys. Rev. Lett.* **123**, 157801 (2019).

- [154] Y.-K. Kim, S. V. Shiyonovskii, and O. D. Lavrentovich, Morphogenesis of defects and tactoids during isotropic–nematic phase transition in self-assembled lyotropic chromonic liquid crystals, *J. Phys.: Condens. Matter* **25**, 404202 (2013).
- [155] V. Jamali, N. Behabtu, B. Senyuk, J. A. Lee, I. I. Smalyukh, P. van der Schoot, and M. Pasquali, Experimental realization of crossover in shape and director field of nematic tactoids, *Phys. Rev. E* **91**, 042507 (2015).
- [156] R. Koizumi, D. Golovaty, A. Alqarni, B.-X. Li, P. J. Sternberg, and O. D. Lavrentovich, Topological transformations of a nematic drop, *Sci. Adv.* **9**, eadf3385 (2023).
- [157] J. Shechter, N. Atzin, A. Mozaffari, R. Zhang, Y. Zhou, B. Strain, L. M. Oster, J. J. De Pablo, and J. L. Ross, Direct observation of liquid crystal droplet configurational transitions using optical tweezers, *Langmuir* **36**, 7074 (2020).
- [158] M. Sadati, J. A. Martínez-Gonzalez, Y. Zhou, N. T. Qazvini, K. Kurtenbach, X. Li, E. Bokusoglu, R. Zhang, N. L. Abbott, J. P. Hernandez-Ortiz *et al.*, Prolate and oblate chiral liquid crystal spheroids, *Sci. Adv.* **6**, eaba6728 (2020).
- [159] C. D. Schimming and J. Viñals, Equilibrium morphology of tactoids in elastically anisotropic nematics, *Soft Matter* **18**, 8024 (2022).
- [160] D. S. Miller, X. Wang, and N. L. Abbott, Design of functional materials based on liquid crystalline droplets, *Chem. Mater.* **26**, 496 (2014).
- [161] W.-S. Kim, J.-H. Im, H. Kim, J.-K. Choi, Y. Choi, and Y.-K. Kim, Liquid Crystalline systems from nature and interaction of living organisms with liquid crystals, *Adv. Mater.* **35**, 2204275 (2023).
- [162] S. V. Lishchuk and C. M. Care, Shape of an isotropic droplet in a nematic liquid crystal: The role of surfactant, *Phys. Rev. E* **70**, 011702 (2004).
- [163] V. Tomar, S. I. Hernandez, N. L. Abbott, J. P. Hernández-Ortiz, and J. J. De Pablo, Morphological transitions in liquid crystal nanodroplets, *Soft Matter* **8**, 8679 (2012).
- [164] H.-G. Lee, S. Munir, and S.-Y. Park, Cholesteric liquid crystal droplets for biosensors, *ACS Appl. Mater. Interfaces* **8**, 26407 (2016).
- [165] J. Jiang and D.-K. Yang, Bipolar to toroidal configuration transition in liquid crystal droplets, *Liq. Cryst.* **45**, 102 (2018).
- [166] J. A. Martínez-González, Y. Zhou, M. Rahimi, E. Bokusoglu, N. L. Abbott, and J. J. de Pablo, Blue-phase liquid crystal droplets, *Proc. Natl. Acad. Sci. USA* **112**, 13195 (2015).
- [167] Y. Zhou, E. Bokusoglu, J. A. Martínez-González, M. Rahimi, T. F. Roberts, R. Zhang, X. Wang, N. L. Abbott, and J. J. De Pablo, Structural transitions in cholesteric liquid crystal droplets, *ACS Nano* **10**, 6484 (2016).
- [168] C. Zhou, P. Yue, and J. J. Feng, The rise of Newtonian drops in a nematic liquid crystal, *J. Fluid Mech.* **593**, 385 (2007).
- [169] R. B. Reboucas, H. A. Faizi, M. J. Miksis, and P. M. Vlahovska, Stationary shapes of axisymmetric vesicles beyond lowest-energy configurations, *Soft Matter* **20**, 2258 (2024).
- [170] A. Kuhnhold and P. van der Schoot, Structure of nematic tactoids of hard rods, *J. Chem. Phys.* **156**, 104501 (2022).
- [171] E. Bokusoglu, M. Bedolla Pantoja, P. C. Mushenheim, X. Wang, and N. L. Abbott, Design of responsive and active (soft) materials using liquid crystals, *Annu. Rev. Chem. Biomol. Eng.* **7**, 163 (2016).
- [172] P.-X. Wang, W. Y. Hamad, and M. J. MacLachlan, Structure and transformation of tactoids in cellulose nanocrystal suspensions, *Nat. Commun.* **7**, 11515 (2016).
- [173] P.-X. Wang and M. J. MacLachlan, Liquid crystalline tactoids: Ordered structure, defective coalescence and evolution in confined geometries, *Philos. Trans. R. Soc. A* **376**, 20170042 (2018).
- [174] B. J. Ortiz, M. E. Boursier, K. L. Barrett, D. E. Manson, D. Amador-Noguez, N. L. Abbott, H. E. Blackwell, and D. M. Lynn, Liquid crystal emulsions that intercept and report on bacterial quorum sensing, *ACS Appl. Mater. Interfaces* **12**, 29056 (2020).
- [175] U. Manna, Y. M. Zavala, N. L. Abbott, and D. M. Lynn, Structured liquid droplets as chemical sensors that function inside living cells, *ACS Appl. Mater. Interfaces* **13**, 42502 (2021).
- [176] Z. Wang, T. Xu, A. Noel, Y.-C. Chen, and T. Liu, Applications of liquid crystals in biosensing, *Soft Matter* **17**, 4675 (2021).

- [177] J. Brugués and D. Needleman, Physical basis of spindle self-organization, *Proc. Natl. Acad. Sci. USA* **111**, 18496 (2014).
- [178] B. Edozie, S. Sahu, M. Pitta, A. Englert, C. F. Do Rosario, and J. L. Ross, Self-organization of spindle-like microtubule structures, *Soft Matter* **15**, 4797 (2019).
- [179] D. Oriola, F. Jülicher, and J. Brugués, Active forces shape the metaphase spindle through a mechanical instability, *Proc. Natl. Acad. Sci. USA* **117**, 16154 (2020).
- [180] F. J. Schwarzendahl, P. Ronceray, K. L. Weirich, and K. Dasbiswas, Self-organization and shape change by active polarization in nematic droplets, *Phys. Rev. Res.* **3**, 043061 (2021).
- [181] W. Conway, R. Kiewisz, G. Fabig, C. P. Kelleher, H.-Y. Wu, M. Anjur-Dietrich, T. Müller-Reichert, and D. J. Needleman, Self-organization of kinetochore-fibers in human mitotic spindles, *Elife* **11**, e75458 (2022).
- [182] F. Lin and C. Wang, Isotropic-nematic phase transition and liquid crystal droplets, *Commun. Pure Appl. Math.* **76**, 1728 (2023).
- [183] A. E. Green and J. E. Adkins, *Large Elastic Deformations* (Clarendon Press, London, 1970).
- [184] D. Barthes-Biesel and J. M. Rallison, The time-dependent deformation of a capsule freely suspended in a linear shear flow, *J. Fluid Mech.* **113**, 251 (1981).
- [185] G. A. Holzapfel, *Nonlinear Solid Mechanics: A Continuum Approach for Engineering Science* (John Wiley & Sons, New York, 2000).
- [186] R. Skalak, A. Tozeren, R. P. Zarda, and S. Chien, Strain energy function of red blood cell membranes, *Biophys. J.* **13**, 245 (1973).
- [187] D. Barthès-biesel, A. Diaz, and E. Dhenin, Effect of constitutive laws for two-dimensional membranes on flow-induced capsule deformation, *J. Fluid Mech.* **460**, 211 (2002).
- [188] J. B. Freund, Numerical simulation of flowing blood cells, *Annu. Rev. Fluid Mech.* **46**, 67 (2014).
- [189] E. A. Evans, A new material concept for the red cell membrane, *Biophys. J.* **13**, 926 (1973).
- [190] C. Pozrikidis, Numerical simulation of the flow-induced deformation of red blood cells, *Ann. Biomed. Eng.* **31**, 1194 (2003).
- [191] D. A. Fedosov, B. Caswell, and G. E. Karniadakis, A multiscale red blood cell model with accurate mechanics, rheology, and dynamics, *Biophys. J.* **98**, 2215 (2010).
- [192] K. Sinha and M. D. Graham, Dynamics of a single red blood cell in simple shear flow, *Phys. Rev. E* **92**, 042710 (2015).
- [193] H. Zhao, A. H. G. Isfahani, L. N. Olson, and J. B. Freund, A spectral boundary integral method for flowing blood cells, *J. Comput. Phys.* **229**, 3726 (2010).
- [194] M. Maleki, B. Seguin, and E. Fried, Kinematics, material symmetry, and energy densities for lipid bilayers with spontaneous curvature, *Biomech. Model. Mechanobiol.* **12**, 997 (2013).
- [195] G. Chagnon, M. Rebouah, and D. Favier, Hyperelastic energy densities for soft biological tissues: A review, *J. Elas.* **120**, 129 (2015).
- [196] P. B. Canham, The minimum energy of bending as a possible explanation of the biconcave shape of the human red blood cell, *J. Theor. Biol.* **26**, 61 (1970).
- [197] W. Helfrich, Elastic properties of lipid bilayers: Theory and possible experiments, *Z. Naturforsch.* **228**, 693 (1973).
- [198] E. A. Evans, Bending resistance and chemically induced moments in membrane bilayers, *Biophys. J.* **14**, 923 (1974).
- [199] T. R. Powers, Dynamics of filaments and membranes in a viscous fluid, *Rev. Mod. Phys.* **82**, 1607 (2010).
- [200] M. Deserno, Fluid lipid membranes: From differential geometry to curvature stresses, *Chem. Phys. Lipids* **185**, 11 (2015).
- [201] H. Ghaedi, L. C. P. Herrera, S. Alshafeay, L. Harris, J. Almodovar, and K. Nayani, Liquid crystalline collagen assemblies as substrates for directed alignment of human Schwann cells, *Soft Matter* (2024), doi: [10.1039/D4SM00534A](https://doi.org/10.1039/D4SM00534A).
- [202] P. Rofouie, D. Pasini, and A. D. Rey, Morphology of elastic nematic liquid crystal membranes, *Soft Matter* **13**, 5366 (2017).
- [203] U. Seifert, Configurations of fluid membranes and vesicles, *Adv. Phys.* **46**, 13 (1997).

- [204] M. Leoni, O. V. Manyuhina, M. J. Bowick, and M. C. Marchetti, Defect driven shapes in nematic droplets: Analogies with cell division, *Soft Matter* **13**, 1257 (2017).
- [205] F. E. Mackay and C. Denniston, Deformable vesicles interacting in a nematic liquid crystal, *Soft Matter* **9**, 5285 (2013).
- [206] T. C. Lubensky and J. Prost, Orientational order and vesicle shape, *J. Phys. II* **2**, 371 (1992).
- [207] H. Shin, M. J. Bowick, and X. Xing, Topological defects in spherical nematics, *Phys. Rev. Lett.* **101**, 037802 (2008).
- [208] V. Vitelli and D. R. Nelson, Nematic textures in spherical shells, *Phys. Rev. E* **74**, 021711 (2006).
- [209] M. A. Bates, G. Skačej, and C. Zannoni, Defects and ordering in nematic coatings on uniaxial and biaxial colloids, *Soft Matter* **6**, 655 (2010).
- [210] T. Lopez-Leon, V. Koning, K. B. S. Devaiah, V. Vitelli, and A. Fernandez-Nieves, Frustrated nematic order in spherical geometries, *Nat. Phys.* **7**, 391 (2011).
- [211] T.-S. Nguyen, J. Geng, R. L. B. Selinger, and J. V. Selinger, Nematic order on a deformable vesicle: Theory and simulation, *Soft Matter* **9**, 8314 (2013).
- [212] M. Nestler, I. Nitschke, H. Löwen, and A. Voigt, Properties of surface Landau–de Gennes Q-tensor models, *Soft Matter* **16**, 4032 (2020).
- [213] D. Jesenek, S. Kralj, R. Rosso, and E. G. Virga, Defect unbinding on a toroidal nematic shell, *Soft Matter* **11**, 2434 (2015).
- [214] P. Sheng, Phase transition in surface-aligned nematic films, *Phys. Rev. Lett.* **37**, 1059 (1976).
- [215] B. G.-G. Chen and R. D. Kamien, Nematic films and radially anisotropic Delaunay surfaces, *Eur. Phys. J. E* **28**, 315 (2009).
- [216] G. Napoli and L. Vergori, Influence of the extrinsic curvature on two-dimensional nematic films, *Phys. Rev. E* **97**, 052705 (2018).
- [217] L. Kondic and L. J. Cummings, Instabilities of nematic liquid crystal films, *Curr. Opin. Colloid Interface Sci.* **55**, 101478 (2021).
- [218] L. Jia, A. Cao, D. Lévy, B. Xu, P. A. Albouy, X. Xing, M. J. Bowick, and M.-H. Li, Smectic polymer vesicles, *Soft Matter* **5**, 3446 (2009).
- [219] X. Xing, H. Shin, M. J. Bowick, Z. Yao, L. Jia, and M.-H. Li, Morphology of nematic and smectic vesicles, *Proc. Natl. Acad. Sci. USA* **109**, 5202 (2012).
- [220] L. S. Hirst, A. Ossowski, M. Fraser, J. Geng, J. V. Selinger, and R. L. B. Selinger, Morphology transition in lipid vesicles due to in-plane order and topological defects, *Proc. Natl. Acad. Sci. USA* **110**, 3242 (2013).
- [221] F. C. MacKintosh and T. C. Lubensky, Orientational order, topology, and vesicle shapes, *Phys. Rev. Lett.* **67**, 1169 (1991).
- [222] J. R. Frank and M. Kardar, Defects in nematic membranes can buckle into pseudospheres, *Phys. Rev. E* **77**, 041705 (2008).
- [223] N. Ramakrishnan, P. B. S. Kumar, and J. H. Ipsen, Membrane-mediated aggregation of curvature-inducing nematogens and membrane tubulation, *Biophys. J.* **104**, 1018 (2013).
- [224] H. Jiang, G. Huber, R. A. Pelcovits, and T. R. Powers, Vesicle shape, molecular tilt, and the suppression of necks, *Phys. Rev. E* **76**, 031908 (2007).
- [225] D. Golovaty, J. A. Montero, and P. Sternberg, Dimension reduction for the Landau-de Gennes model on curved nematic thin films, *J. Nonlin. Sci.* **27**, 1905 (2017).
- [226] I. Nitschke, M. Nestler, S. Praetorius, H. Löwen, and A. Voigt, Nematic liquid crystals on curved surfaces: A thin film limit, *Proc. R. Soc. A.* **474**, 20170686 (2018).
- [227] I. Nitschke, S. Reuther, and A. Voigt, Liquid crystals on deformable surfaces, *Proc. R. Soc. A* **476**, 20200313 (2020).
- [228] S. C. Glotzer and M. J. Solomon, Anisotropy of building blocks and their assembly into complex structures, *Nat. Mater.* **6**, 557 (2007).
- [229] Z. Li, Q. Fan, and Y. Yin, Colloidal self-assembly approaches to smart nanostructured materials, *Chem. Rev.* **122**, 4976 (2022).
- [230] L. A. Hoffmann, L. N. Carenza, J. Eckert, and L. Giomi, Theory of defect-mediated morphogenesis, *Sci. Adv.* **8**, eabk2712 (2022).

- [231] D. Khoromskaia and G. Salbreux, Active morphogenesis of patterned epithelial shells, *eLife* **12**, e75878 (2023).
- [232] L. Mesarec, W. Gózdź, V. Kralj-Iglič, S. Kralj, and A. Iglič, Coupling of nematic in-plane orientational ordering and equilibrium shapes of closed flexible nematic shells, *Sci. Rep.* **13**, 10663 (2023).
- [233] U. Seifert, K. Berndl, and R. Lipowsky, Shape transformations of vesicles: Phase diagram for spontaneous-curvature and bilayer-coupling models, *Phys. Rev. A* **44**, 1182 (1991).
- [234] A. Guckenberger and S. Gekle, Theory and algorithms to compute Helfrich bending forces: A review, *J. Phys.: Condens. Matter* **29**, 203001 (2017).
- [235] A. Segatti, M. Snarski, and M. Veneroni, Analysis of a variational model for nematic shells, *Math. Models Methods Appl. Sci.* **26**, 1865 (2016).
- [236] G. Canevari and A. Segatti, Variational analysis of nematic shells, in *Trends in Applications of Mathematics to Mechanics* (Springer, Berlin, 2018), pp. 81–102.
- [237] G. Canevari and A. Segatti, Defects in nematic shells: A γ -convergence discrete-to-continuum approach, *Arch. Ration. Mech.* **229**, 125 (2018).
- [238] M. Warner and E. M. Terentjev, *Liquid Crystal Elastomers*, Vol. 120 (Oxford University Press, Oxford, 2007).
- [239] S. W. Ula, N. A. Traugott, R. H. Volpe, R. R. Patel, K. Yu, and C. M. Yakacki, Liquid crystal elastomers: An introduction and review of emerging technologies, *Liq. Cryst. Rev.* **6**, 78 (2018).
- [240] A. Agrawal, P. Luchette, P. Palfy-Muhoray, S. L. Biswal, W. G. Chapman, and R. Verduzco, Surface wrinkling in liquid crystal elastomers, *Soft Matter* **8**, 7138 (2012).
- [241] H. Soni, R. A. Pelcovits, and T. R. Powers, Wrinkling of a thin film on a nematic liquid-crystal elastomer, *Phys. Rev. E* **94**, 012701 (2016).
- [242] A. Goriely and L. A. Mihai, Liquid crystal elastomers wrinkling, *Nonlinearity* **34**, 5599 (2021).
- [243] T. J. White and D. J. Broer, Programmable and adaptive mechanics with liquid crystal polymer networks and elastomers, *Nat. Mater.* **14**, 1087 (2015).
- [244] C. Mostajeran, M. Warner, T. H. Ware, and T. J. White, Encoding Gaussian curvature in glassy and elastomeric liquid crystal solids, *Proc. R. Soc. A* **472**, 20160112 (2016).
- [245] H. Aharoni, Y. Xia, X. Zhang, R. D. Kamien, and S. Yang, Universal inverse design of surfaces with thin nematic elastomer sheets, *Proc. Natl. Acad. Sci. USA* **115**, 7206 (2018).
- [246] T. Gibaud, E. Barry, M. J. Zakhary, M. Henglin, A. Ward, Y. Yang, C. Berciu, R. Oldenbourg, M. F. Hagan, D. Nicastro *et al.*, Reconfigurable self-assembly through chiral control of interfacial tension, *Nature (Lond)* **481**, 348 (2012).
- [247] L. L. Jia, M. J. Zakhary, Z. Dogic, R. A. Pelcovits, and T. R. Powers, Chiral edge fluctuations of colloidal membranes, *Phys. Rev. E* **95**, 060701(R) (2017).
- [248] L. Ding, R. A. Pelcovits, and T. R. Powers, Deformation and orientational order of chiral membranes with free edges, *Soft Matter* **17**, 6580 (2021).
- [249] A. Khanra, L. L. Jia, N. P. Mitchell, A. Balchunas, R. A. Pelcovits, T. R. Powers, Z. Dogic, and P. Sharma, Controlling the shape and topology of two-component colloidal membranes, *Proc. Natl. Acad. Sci. USA* **119**, e2204453119 (2022).
- [250] L. Ding, R. A. Pelcovits, and T. R. Powers, Chiral fluid membranes with orientational order and multiple edges, *Soft Matter* **19**, 8453 (2023).
- [251] F. C. Keber, E. Loiseau, T. Sanchez, S. J. DeCamp, L. Giomi, M. J. Bowick, M. C. Marchetti, Z. Dogic, and A. R. Bausch, Topology and dynamics of active nematic vesicles, *Science* **345**, 1135 (2014).
- [252] L. Metselaar, J. L. Yeomans, and A. Doostmohammadi, Topology and morphology of self-deforming active shells, *Phys. Rev. Lett.* **123**, 208001 (2019).
- [253] M. Firouznia and D. Saintillan, Self-organized dynamics of a viscous drop with interfacial nematic activity, [arXiv:2404.11729](https://arxiv.org/abs/2404.11729).
- [254] C. Zhu, S. Saintillan, and A. Chern, Active nematic fluids on Riemannian 2-manifolds, [arXiv:2405.06044](https://arxiv.org/abs/2405.06044).
- [255] G. Salbreux, F. Jülicher, J. Prost, and A. Callan-Jones, Theory of nematic and polar active fluid surfaces, *Phys. Rev. Res.* **4**, 033158 (2022).

- [256] T. B. Saw, A. Doostmohammadi, V. Nier, L. Kocgozlu, S. Thampi, Y. Toyama, P. Marcq, C. T. Lim, J. M. Yeomans, and B. Ladoux, Topological defects in epithelia govern cell death and extrusion, *Nature (Lond.)* **544**, 212 (2017).
- [257] F. Vafa and L. Mahadevan, Active nematic defects and epithelial morphogenesis, *Phys. Rev. Lett.* **129**, 098102 (2022).
- [258] J. Zhang, N. Yang, P. K. Kreeger, and J. Notbohm, Topological defects in the mesothelium suppress ovarian cancer cell clearance, *APL Bioeng.* **5**, 036103 (2021).
- [259] K. Kawaguchi, R. Kageyama, and M. Sano, Topological defects control collective dynamics in neural progenitor cell cultures, *Nature (Lond.)* **545**, 327 (2017).
- [260] A. DeBenedictis, T. J. Atherton, A. L. Rodarte, and L. S. Hirst, Modeling deformation and chaining of flexible shells in a nematic solvent with finite elements on an adaptive moving mesh, *Phys. Rev. E* **97**, 032701 (2018).
- [261] A. DeBenedictis and T. J. Atherton, Shape minimisation problems in liquid crystals, *Liq. Cryst.* **43**, 2352 (2016).
- [262] A. DeBenedictis, Shape Deformation through Geometric Frustration of Liquid Crystals, Ph.D. thesis, Tufts University, 2018.
- [263] R. D. Kamien, The geometry of soft materials: A primer, *Rev. Mod. Phys.* **74**, 953 (2002).
- [264] D. Varadharajan, K. Nayani, C. Zippel, E. Spuling, K. C. Cheng, S. Sarangarajan, S. Roh, J. Kim, V. Trouillet, S. Bräse *et al.*, Surfaces decorated with enantiomorphically pure polymer nanohelices via hierarchical chirality transfer across multiple length scales, *Adv. Mater.* **34**, 2108386 (2022).
- [265] S. Roh, J. Kim, D. Varadharajan, J. Lahann, and N. L. Abbott, Sharing of strain between nanofiber forests and liquid crystals leads to programmable responses to electric fields, *Adv. Funct. Mat.* **32**, 2200830 (2022).
- [266] J. Chrispell and L. Fauci, Peristaltic pumping of solid particles immersed in a viscoelastic fluid, *Math. Model. Nat. Phenom.* **6**, 67 (2011).
- [267] D. Devendran and C. S. Peskin, An immersed boundary energy-based method for incompressible viscoelasticity, *J. Comput. Phys.* **231**, 4613 (2012).
- [268] R. D. Guy and B. Thomases, Computational challenges for simulating strongly elastic flows in biology, in *Complex Fluids in Biological Systems* (Springer, Berlin, 2015), pp. 359–397.
- [269] C. Fernandes, S. A. Faroughi, O. S. Carneiro, J. M. Nóbrega, and G. H. McKinley, Fully-resolved simulations of particle-laden viscoelastic fluids using an immersed boundary method, *J. Non-Newton. Fluid Mech.* **266**, 80 (2019).
- [270] C. Gruninger, A. Barrett, F. Fang, M. G. Forest, and B. E. Griffith, Benchmarking the immersed boundary method for viscoelastic flows, *J. Comput. Phys.* **506**, 112888 (2024).
- [271] J. Teran, L. Fauci, and M. Shelley, Viscoelastic fluid response can increase the speed and efficiency of a free swimmer, *Phys. Rev. Lett.* **104**, 038101 (2010).
- [272] M. S. Krieger, S. E. Spagnolie, and T. R. Powers, Swimming with small and large amplitude waves in a confined liquid crystal, *J. Non-Newton. Fluid Mech.* **273**, 104185 (2019).
- [273] Z. Lin, S. Chen, and T. Gao, Q-tensor model for undulatory swimming in lyotropic liquid crystal polymers, *J. Fluid Mech.* **921**, A25 (2021).
- [274] D. B. Stein, R. D. Guy, and B. Thomases, Immersed boundary smooth extension: A high-order method for solving PDE on arbitrary smooth domains using Fourier spectral methods, *J. Comput. Phys.* **304**, 252 (2016).
- [275] B. E. Griffith and N. A. Patankar, Immersed methods for fluid–structure interaction, *Annu. Rev. Fluid Mech.* **52**, 421 (2020).
- [276] J. P. Borthagaray, R. H. Nochetto, and S. W. Walker, A structure-preserving FEM for the uniaxially constrained Q-tensor model of nematic liquid crystals, *Numer. Math.* **145**, 837 (2020).
- [277] P. Yue, J. J. Feng, C. Liu, and J. Shen, A diffuse-interface method for simulating two-phase flows of complex fluids, *J. Fluid Mech.* **515**, 293 (1999).
- [278] C. Zhou, P. Yue, and J. J. Feng, Dynamic simulation of droplet interaction and self-assembly in a nematic liquid crystal, *Langmuir* **24**, 3099 (2008).

- [279] A. Saadat, C. J. Guido, G. Iaccarino, and E. S. G. Shaqfeh, Immersed-finite-element method for deformable particle suspensions in viscous and viscoelastic media, *Phys. Rev. E* **98**, 063316 (2018).
- [280] S. V. Lishchuk, C. M. Care, and I. Halliday, A lattice Boltzmann scheme for a nematic–isotropic interface, *J. Phys.: Condens. Matter* **16**, S1931 (2004).
- [281] N. Sulaiman, D. Marenduzzo, and J. M. Yeomans, Lattice Boltzmann algorithm to simulate isotropic-nematic emulsions, *Phys. Rev. E* **74**, 041708 (2006).
- [282] J. Ma, Z. Wang, J. Young, J. C. S. Lai, Y. Sui, and F.-B. Tian, An immersed boundary-lattice Boltzmann method for fluid-structure interaction problems involving viscoelastic fluids and complex geometries, *J. Comput. Phys.* **415**, 109487 (2020).
- [283] A. H. Raffiee, S. Dabiri, and A. M. Ardekani, Suspension of deformable particles in newtonian and viscoelastic fluids in a microchannel, *Microfluid. Nanofluid.* **23**, 22 (2019).
- [284] N. O. Jaensson, P. D. Anderson, and J. Vermant, Computational interfacial rheology, *J. Non-Newton. Fluid Mech.* **290**, 104507 (2021).
- [285] O. D. Lavrentovich, Design of nematic liquid crystals to control microscale dynamics, *Liq. Cryst. Rev.* **8**, 59 (2020).
- [286] R. W. Ruhwandl and E. M. Terentjev, Friction drag on a particle moving in a nematic liquid crystal, *Phys. Rev. E* **54**, 5204 (1996).
- [287] J. C. Loudet, P. Hanusse, and P. Poulin, Stokes drag on a sphere in a nematic liquid crystal, *Science* **306**, 1525 (2004).
- [288] H. Stark and D. Venzki, Non-linear Stokes drag of spherical particles in a nematic solvent, *Europhys. Lett.* **57**, 60 (2002).
- [289] M. Gómez-González and J. C. del Álamo, Flow of a viscous nematic fluid around a sphere, *J. Fluid Mech.* **725**, 299 (2013).
- [290] M. D. Graham, *Microhydrodynamics, Brownian Motion, and Complex Fluids*, Vol. 58 (Cambridge University Press, Cambridge, UK, 2018).
- [291] C. Peng, T. Turiv, Y. Guo, Q.-H. Wei, and O. D. Lavrentovich, Command of active matter by topological defects and patterns, *Science* **354**, 882 (2016).
- [292] M. M. Genkin, A. Sokolov, O. D. Lavrentovich, and I. S. Aranson, Topological defects in a living nematic ensnare swimming bacteria, *Phys. Rev. X* **7**, 011029 (2017).
- [293] M. S. Krieger, M. A. Dias, and T. R. Powers, Microscale locomotion in a nematic liquid crystal, *Soft Matter* **11**, 9115 (2015).
- [294] A. Sokolov, S. Zhou, O. D. Lavrentovich, and I. S. Aranson, Individual behavior and pairwise interactions between microswimmers in anisotropic liquid, *Phys. Rev. E* **91**, 013009 (2015).
- [295] S. Zhou, O. Tovkach, D. Golovaty, A. Sokolov, I. S. Aranson, and O. D. Lavrentovich, Dynamic states of swimming bacteria in a nematic liquid crystal cell with homeotropic alignment, *New J. Phys.* **19**, 055006 (2017).
- [296] J. Prost, F. Jülicher, and J.-F. Joanny, Active gel physics, *Nat. Phys.* **11**, 111 (2015).
- [297] G. J. Elfring and E. Lauga, Theory of locomotion through complex fluids, in *Complex Fluids in Biological Systems* (Springer, Berlin, 2015), pp. 283–317.
- [298] P. E. Arratia, Life in complex fluids: Swimming in polymers, *Phys. Rev. Fluids* **7**, 110515 (2022).
- [299] S. E. Spagnolie and P. T. Underhill, Swimming in complex fluids, *Annu. Rev. Condens. Matter Phys.* **14**, 1 (2023).
- [300] C. Krüger, G. Klös, C. Bahr, and C. C. Maass, Curling liquid crystal microswimmers: A cascade of spontaneous symmetry breaking, *Phys. Rev. Lett.* **117**, 048003 (2016).
- [301] K. Nayani, U. M. Córdova-Figueroa, and N. L. Abbott, Steering active emulsions with liquid crystals, *Langmuir* **36**, 6948 (2020).
- [302] C. C. Maass, C. Krüger, S. Herminghaus, and C. Bahr, Swimming droplets, *Annu. Rev. Condens. Matter Phys.* **7**, 171 (2016).
- [303] S. Michelin, Self-propulsion of chemically active droplets, *Annu. Rev. Fluid Mech.* **55**, 77 (2023).
- [304] J. Li, M. Dao, C. T. Lim, and S. Suresh, Spectrin-level modeling of the cytoskeleton and optical tweezers stretching of the erythrocyte, *Biophys. J.* **88**, 3707 (2005).